LIQUID CRYSTAL COLLOIDAL DISPERSIONS

HOLGER STARK
Fachbereich Physik, Universität Konstanz, D-78457 Konstanz, Germany

AND

ANAMARIJA BORŠTNIK AND SLOBODAN ŽUMER
Department of Physics, University of Ljubljana, 1000 Ljubljana, Slovenia

1. Introduction

In colloidal dispersions particles whose size ranges from 10 nm to 10 μm are suspended in a host medium. One distinguishes between emulsions, where surfactant-coated liquid droplets are dispersed in a fluid environment, colloidal suspensions, where the particles are solid, and aerosoles, with fluid or solid particles floating in a gaseous phase. As such these systems can be found in our everyday life, *e.g.*, in food, with milk being the best-known fat-in-water emulsion, in drugs, cosmetics, paints, and ink. With berg lakes in the Canadian Rocky mountains or just simple fog, nature also creates its colloidal dispersions. It is of vital interest to keep the particles in the dispersed state since in the aggregated state the characteristics of colloidal systems change dramatically. There exists a whole zoo of interactions between particles whose delicate balance determines the stability of a colloidal dispersion. Conventionally, the attractive van der Waals force is compensated by a screened Coulombic or steric interaction [1]. Recently, fluctuation-induced Casimir forces either in binary fluids close to the critical point [2, 3] or in liquid crystals [4, 5, 6, 7] and also depletion forces in binary mixtures of small and large spheres [1, 8, 9, 10] have attracted a lot of interest. Furthermore, colloidal dispersions are used to study such fundmental questions as the Brownian motion of suspended particles in connection with long-time tails in the velocity auto-correlation function [11, 12, 13] and with regard to hydrodynamic interactions [1, 14]. The aggregation of particles leads to fractal structures [15, 16, 17]. If the particles

carry an additional dipole moment, as in electrorheological fluids or in magnetic emulsions, characteristic chain structures occur under the influence of external fields [18, 19].

Here we deal with the suspension of particles in an anisotropic fluid, *i.e.*, a nematic liquid crystal. New types of colloidal forces arrive as we review in the following. In the nematic phase they are mediated by elastic distortions of the director field and thus have long range. On contrary, above the nematic-isotropic phase transition temperature T_{NI} they are governed by a nematic wetting layer at the surface of the particles and are therefore of short range. Furthermore, in the nematic phase topological point and line defects in the director field occur which strongly determine the physics of liquid crystal colloidal dispersions. Both, the nematic wetting layer above T_{NI} and the core of a defect in the director field require the alignment tensor $\mathbf{Q}$ as generalized order parameter to describe the liquid crystalline ordering.

In multiple nematic emulsions, *e.g.*, surfactant-coated water droplets are dispersed in large nematic drops which are surrounded by the water phase [20, 21]. Surprisingly, as observed by polarizing microscopy, the water droplets form chains. Such structures have only been seen, so far, under the influence of external fields, as mentioned above. Moreover, a high magnification of the chains revealed that the water droplets did not touch each other. All the observations can be explained by the presence of the nematic host medium below T_{NI} taking into account homeotropic boundary conditions at all the surfaces. Figure 1 illustrates that the water droplets are separated by the presence of hyperbolic point defects in the director field which mediate a strong repulsion between the droplets. As soon as the host medium is heated into the isotropic phase, the water droplets start to diffuse around and coalesce upon touching each other. This effect indicates the existence of a flocculation transition.

Multiple nematic emulsions are an ideal laboratory to study topological point defects [22, 23, 24, 25]. Their charge q is given by the number of times the unit sphere is wrapped by all the directors on a surface enclosing the defect core. The sign of q has no meaning due to the head-tail symmetry of the orientational order. Note that the directors close to a point defect are reversed if the defect is moved around a $\pm 1/2$ disclination line [24]. Therefore, source and sink fields are equivalent. In addition, two point charges q_1 and q_2 can give the respective total charges $q_1 + q_2$ or $|q_1 - q_2|$ depending on the global boundary conditions. It is obvious that the large nematic drop and each water droplet in Fig. 1 carry a charge $q = +1$. One single water droplet fits perfectly into the nematic drop. Every additional water droplet has to be accompanied by a defect structure of charge $q = +1$ so that the total charge of the nematic drop remains $q = +1$. In Fig. 1 this is achieved

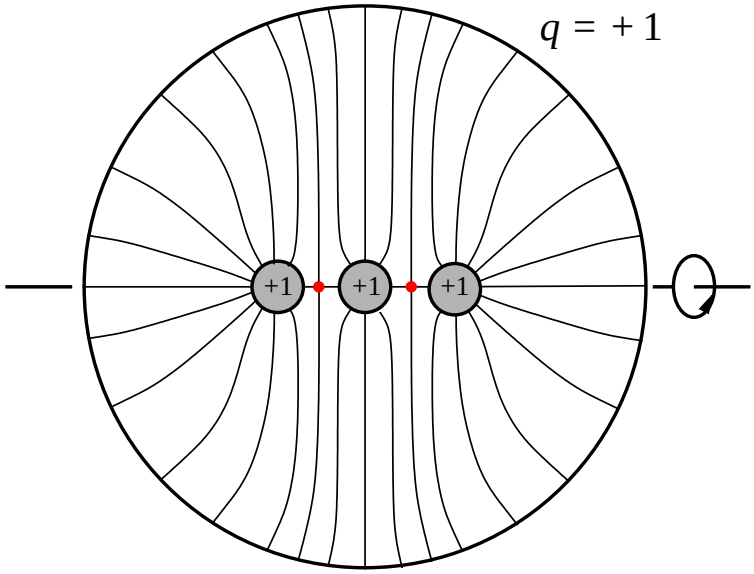

Figure 1. The director field lines of a nematic drop containing a string of three water droplets. Each droplet stands for a radial point defect of charge $q = +1$. To achieve the total charge $q = +1$ of the nematic drop, the water droplets are separated by hyperbolic point defects of charge $q = +1$.

by placing hyperbolic point defects between the water droplets. They can be identified as black dots under the polarizing miscroscope. A spherical particle with an attached hyperbolic point defect has a total charge $q = 0$ as we will illustrate below.

In the following we shortly review some work of the authors [20, 26, 27, 28, 29, 30, 31, 32] related to liquid crystal colloidal dispersions. It is not our intention to give a complete overview of the field and an extensive list of references. They can be found in Refs. [33, 32].

In section 2 we first address colloidal dispersions in a nematic solvent. They exhibit long range two-particle interactions. In Subsection 2.1 we give an overview of the calculational methods which are employed to handle such systems. For the understanding of nematic colloidal dispersions, it is helpful to first consider the simplest possible configuration consisting of one particle and a uniform director field at infinity. This system already allows for several structures which we discuss in Subsection 2.2. Then, in Subsection 2.3, we shortly address the two-particle interactions in a nematic solvent. Finally, in Subsection 2.4, we summarize numerical work on colloidal dispersions in complex geometries concentrating on the structures seen in multiple nematic emulsions. In Section 3 we address colloidal dispersions where the host medium is already in the isotropic state but close

to the nematic-isotropic phase transition. Interactions in these systems are short ranged so that their behavior is similar to classical colloidal dispersions. Furthermore, they are strongly attractive close to T_{NI}, and they can be switched off by raising temperature. In Subsection 3.2 we show how the Landau-de Gennes phenomenological theory is used to describe partial liquid crystal ordering at temperatures above T_{NI}. From such a study, the properties of the two-particle interaction mediated by the liquid crystal can be deduced. We analyze the behavior of an isotropic liquid crystal colloidal dispersion and show that neutral micron-sized spherical particles do not stay dispersed but rather form aggregates. Subsection 3.3 is dedicated to an isotropic liquid crystal dispersion of equally charged particles which stay dispersed well above T_{NI}. We demonstrate that the liquid crystal mediated interaction can induce a sharp flocculation transition from the dispersed into the flocculated state by lowering temperature.

2. Colloidal Dispersions in a Nematic Solvent

2.1. WHAT IS THE DIRECTOR FIELD?

To understand the physics of nematic colloidal dispersions, it is crucial to determine the director field $\mathbf{n}(\mathbf{r})$ around the particles. It follows from a minimization of the relevant free energy as a functional of $\mathbf{n}(\mathbf{r})$.

2.1.1. *Free Energy*

The total free energy consists of bulk and surface terms,

$$F_{\mathbf{n}} = F_{el} + F_{24} + F_H + F_S = \int d^3r \, (f_{el} + f_{24} + f_H) + \int dS f_S \ . \qquad (1)$$

Here $f_{el} + f_{24}$ stands for the Oseen-Zöcher-Frank free energy density [34, 35, 36, 37] with

$$f_{el} = \frac{1}{2}[K_1(\mathrm{div}\mathbf{n})^2 + K_2(\mathbf{n} \cdot \mathrm{curl}\mathbf{n})^2 + K_3(\mathbf{n} \times \mathrm{curl}\mathbf{n})^2] \qquad (2)$$

and

$$f_{24} = -\frac{K_{24}}{2}\mathrm{div}(\mathbf{n}\mathrm{div}\mathbf{n} + \mathbf{n} \times \mathrm{curl}\mathbf{n}) \ . \qquad (3)$$

The coefficients K_1, K_2, K_3, and K_{24} denote, respectively, the *splay*, *twist*, *bend*, and *saddle-splay* elastic constants. The saddle-splay term is a pure divergence and can be transformed into integrals over all surfaces of the system,

$$F_{24} = -\frac{1}{2}K_{24} \int d\mathbf{S} \cdot (\mathbf{n}\mathrm{div}\mathbf{n} + \mathbf{n} \times \mathrm{curl}\mathbf{n}) \ , \qquad (4)$$

where it prefers the formation of a saddle-like structure. A further surface term with a free energy density $K_{13}\,\mathrm{div}(\mathbf{n}\mathrm{div}\mathbf{n})$ will not be considered in the following [38, 39].

In the one-constant approximation, $K = K_1 = K_2 = K_3$, the Frank free energy takes the form

$$F_{el} = \frac{K}{2}\int d^3r(\nabla_i n_j)^2 + \frac{K-K_{24}}{2}\int d\mathbf{S}\cdot(\mathbf{n}\mathrm{div}\mathbf{n} + \mathbf{n}\times\mathrm{curl}\mathbf{n}) \ . \qquad (5)$$

It is often used to obtain a basic understanding of a system without having to deal with effects due to elastic anisotropy. The bulk term is equivalent to the non-linear sigma model in statistical field theory [40, 25] or the continuum description of the exchange interaction in a ferromagnet [41].

The magnetic free energy density f_H reads

$$f_H = -\frac{\Delta\chi}{2}[(\mathbf{n}\cdot\mathbf{H})^2 - H^2] \ , \qquad (6)$$

where the magnetic anisotropy $\Delta\chi = \chi_{||} - \chi_\perp$ is defined as the difference of the two essential magnetic susceptibilities $\chi_{||}$ and $\chi_\perp$ for magnetic fields applied, respectively, parallel or perpendicular to the director. It is positive and typically of the order of 10^{-7} [37]. By adding a term $-\Delta\chi H^2/2$ on the right-hand side of Eq. (6), we shift the reference point in order that the magnetic free energy of a completely aligned director field is zero. This will be useful in Subsection 2.2 where the free energy of the infinitely extended director field around a single particle is calculated. The balance between elastic and magnetic torques on the director defines an important length scale, the magnetic coherence length

$$\xi_H = \sqrt{\frac{K_3}{\Delta\chi H^2}} \ . \qquad (7)$$

Suppose the director is planarly anchored at a wall, and a magnetic field is applied perpendicular to it. Then ξ_H gives the distance from the wall that is needed to orient the director along the applied field [37]. The coherence length tends to infinity for $H \to 0$.

Finally, the surface free energy of Rapini-Papoular is employed to take into account the anchoring of the director at boundaries:

$$f_S = \frac{W}{2}[1 - (\mathbf{n}\cdot\hat{\boldsymbol{\nu}})^2] \ . \qquad (8)$$

The unit vector $\hat{\boldsymbol{\nu}}$ denotes some preferred orientation of the director at the surface, and W is the coupling constant. It varies in the range $10^{-7} - 10^{-3}$

J/m^2 as reviewed by Blinov *et al.* [42]. From a comparison between the Frank free energy and the surface energy, one arrives at the extrapolation length [37]

$$\xi_S = \frac{K_3}{W} \ . \tag{9}$$

It signifies the strength of the anchoring. Take a particle of radius a in a nematic environment with an uniform director field at infinity (see Subsection 2.2.) The Frank free energy of this system is proportional to $K_3 a$ whereas the surface energy scales as Wa^2. At *strong* anchoring, *i.e.*, for $Wa^2 \gg K_3 a$ or $\xi_S \ll a$, the energy to turn the director away from its preferred direction $\hat{\boldsymbol{\nu}}$ at the whole surface would be much larger than the bulk energy. Therefore, it is preferable for the system that the director points along $\hat{\boldsymbol{\nu}}$. However, $\mathbf{n}$ can deviate from $\hat{\boldsymbol{\nu}}$ in an area of order $\xi_S a$. In Subsection 2.2.4 we will use this argument to explain a ring configuration around the particle. *Rigid* anchoring is realized for $\xi_S \to 0$. Finally, $\xi_S \gg a$ means *weak* anchoring, where the influence of the surface is minor. Since in our discussion we have always referred ξ_S to the radius a, it is obvious that the strength of the anchoring is not an absolute quantity but depends on characteristic length scales of the system.

2.1.2. *Minimization procedures*

The director field $\mathbf{n}(\mathbf{r})$ in a given geometry follows from a minimization of the total free energy $F_{\mathbf{n}} = F_{el} + F_{24} + F_H + F_S$ under the constraint that $\mathbf{n}$ is a unit vector:

$$\delta F_{\mathbf{n}} = 0 \qquad \text{with} \qquad \mathbf{n} \cdot \mathbf{n} = 1 \ . \tag{10}$$

Even in the one-constant approximation and under the assumption of rigid anchoring of the director at the boundaries, this is a difficult problem to solve because of the additional constraint. Typically, full analytical solutions only exist for one-dimensional problems, *e.g.*, for the description of the Fréedericksz transition [43, 37], or in two dimensions when certain symmetries are assumed [26]. To handle the constraint, one can use a Lagrange parameter or introduce an appropriate parametrization for the director, *e.g.*, a tilt (Θ) and twist (Φ) angle, so that the director in the local coordinate basis takes the form

$$\mathbf{n} = (\sin\Theta\cos\Phi, \sin\Theta\sin\Phi, \cos\Theta) \ . \tag{11}$$

If an accurate analytical determination of the director field is not possible, there are two strategies. First, an ansatz function is constructed that fulfills the boundary conditions and contains free parameters. Then, the

director field follows from a minimization of the total free energy in the restricted space of functions with respect to the free parameters. This strategy was successfully applied to the director field around a single spherical particle [20, 26]

Here we concentrate on numerical solutions of the Euler-Lagrange equations corresponding to the variational problem formulated in Eq. (10). They are equivalent to functional derivatives of $F_{\mathbf{n}}[\Theta, \Phi]$, where we use the tilt and twist angle of Eq. (11) to parametrize the director:

$$\frac{\delta F_{\mathbf{n}}}{\delta \Theta} = \frac{\delta F_{\mathbf{n}}}{\delta n_i} \frac{\partial n_i}{\partial \Theta} = 0 \tag{12}$$

$$\frac{\delta F_{\mathbf{n}}}{\delta \Phi} = \frac{\delta F_{\mathbf{n}}}{\delta n_i} \frac{\partial n_i}{\partial \Phi} = 0 \ . \tag{13}$$

Einstein's summation convention over repeated indices is used. To arrive at the equations above for $\Theta(\mathbf{r})$ and $\Phi(\mathbf{r})$, we have employed a chain rule for functional derivatives [27]. These chain rules are useful in numerical problems since they allow to write the Euler-Lagrange equations, which can be quite complex, in a more compact form. For example, the bulk and surface equations that are solved in Subsection 2.2 for a single spherical particle could only be calculated with the help of the algebraic program Maple after applying the chain rules.

Typically, a starting configuration for the director field is taken and relaxed on a grid via the Newton-Gauss-Seidel method [44]. It is equivalent to Newton's iterative way of determining the zeros of a function but now generalized to functionals. We illustrate it here for the tilt angle Θ:

$$\Theta^{\text{new}}(\mathbf{r}) = \Theta^{\text{old}}(\mathbf{r}) - \frac{\delta F_{\mathbf{n}}/\delta\Theta(\mathbf{r})}{\delta^2 F_{\mathbf{n}}/\delta\Theta^2(\mathbf{r})} \ . \tag{14}$$

There are two possibilities to implement the method numerically. Both will be used in the following subsections. In the first case the grid for the numerical investigation is defined by the coordinate lines. To determine, e.g., the axially symmetric director field around a spherical particle in Subsection 2.2, it is appropriate to choose spherical coordinates consisting of the radial distance r and the polar angle θ. Then the boundary of the integration area coincides with the coordinate line $r = 1$. By using a modified radial coordinate $\rho = 1/r^2$, the infinitly extended region around the particle is mapped onto the unit sphere, *i.e.*, a region of finite extent. The director $\mathbf{n}$ is written in the local spherical coordinate basis $(\mathbf{e}_r, \mathbf{e}_\theta, \mathbf{e}_\phi)$ according to Eq. (11). Following the chain rules (12) and (13) and with the help of the algebraic program Maple, the Euler-Lagrange equations are determined analytically. Then, they are discretized by the method of finite differences for a discrete

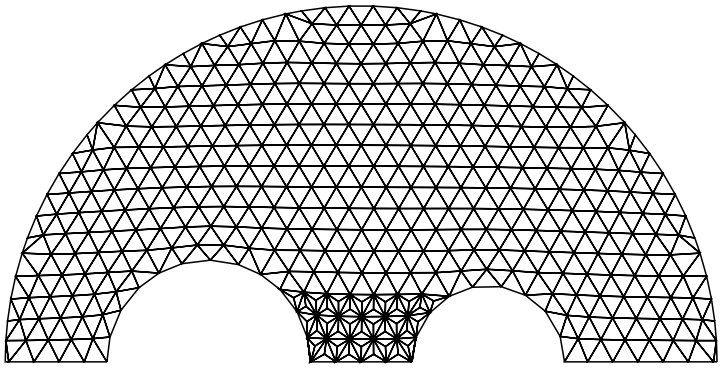

Figure 2. Triangulation of the integration area to simulate a chain of two water droplets in a big nematic drop under the assumption of rotational symmetry about the chain axis. Between the small spheres a refined net of triangles is chosen.

set of grid points $\mathbf{r}$[44]. Finally, $\delta^2 F_{\mathbf{n}}/\delta\Theta^2(\mathbf{r})$ is calculated numerically as the derivative of $\delta F_{\mathbf{n}}/\delta\Theta(\mathbf{r})$ with respect to $\Theta(\mathbf{r})$ at the grid point $\mathbf{r}$ (for further details see Ref. [27]).

If the geometry of the system is more complex, the method of finite elements is appropriate. In Subsection 2.4, the chaining of two water droplets in a big nematic drop is investigated in analogy to Fig. 1. Assuming rotational symmetry about the chain axis, the relevant integration volume is two dimensional (see Fig. 2). It is subdivided into *finite elements*, which in the present case are triangles. In doing so, the boundaries of the complex geometry are well approximated by polygons. Between the two spheres in Fig. 2 a refinement of the grid is chosen to better approximate the hyperbolic point defect. The free energy $F_{\mathbf{n}}$ is discretized on the triangular grid (for details see [28]) and then minimized with the help of the Newton-Gauss-Seidel method. Both the first and second derivatives in Eq. (14) are performed numerically with respect to $\Theta(\mathbf{r})$ at the grid point $\mathbf{r}$.

2.2. ONE-PARTICLE PROPERTIES

In this subsection we ask which director field configurations do occur when one spherical particle that prefers a radial anchoring of the director at its surface is placed into a nematic solvent uniformly aligned at infinity. This constitutes the simplest problem one can think of, and it is a guide to the understanding of more complex situations.

2.2.1. *The Three Possible Configurations*

If the directors are rigidly anchored at the surface, the particle carries a topological charge $q = 1$. Because of the boundary conditions at infinity,

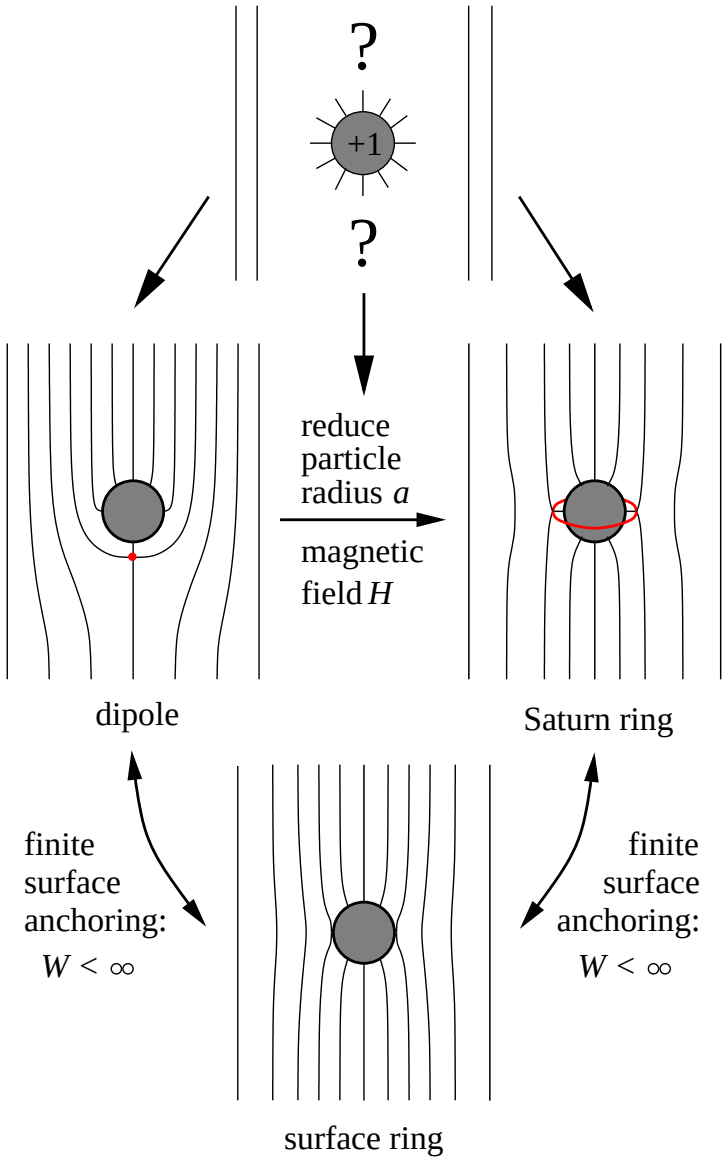

Figure 3. A spherical particle with a preferred homeotropic anchoring at its surface that is placed into a uniformly aligned nematic liquid crystal exhibits three possible structures: the dipole configuration where the particle is accompanied by a hyperbolic hedgehog, the Saturn-ring configuration where the particle is surrounded by a $-1/2$ disclination ring at the equator, and the surface-ring configuration.

the total charge of the whole system is zero; therefore, the particle must nucleate a further defect in its nematic environment. One possibility is a dipolar strucure where the particle and a hyperbolic hedgehog form a tightly bound object which we call *dipole* for short (see Fig. 3) [20, 46, 26, 45, 27]. The topological charges +1 of a radial hedgehog, represented by the particle, and of a hyperbolic point defect "add up" to a total charge of zero. The dipole configuration was thoroughly studied with the help of ansatz functions which were motivated by the electric field solution of the electrostatic analogue: a charged metal sphere placed into a uniform electric field [20, 26]. The outcome of the investigation was that the defect sits close to the spherical particle and that thermal fluctuations of its position are invisibly small [20, 26]. The hyperbolic hedgehog can be opened up to a topologically equivalent $-1/2$ disclination ring. When moved to the symmetric position, where it encircles the spherical particle at the equator (see Fig. 3), the *Saturn-ring* configuration occurs [47, 48, 46, 26, 45, 27]. In the following, it is demonstrated that the transition to the Saturn ring occurs for decreasing particle size and when a magnetic field is applied. The presented calculations show that a non-symmetric position of the defect ring is never stable. When the surface anchoring strength W is lowered (see Fig. 3), the core of the disclination ring prefers to sit directly at the surface of the particle [46, 27]. For sufficiently low W, the director field becomes smooth everywhere, and a ring of tangentially oriented directors is located at the equator of the sphere [48, 46, 45, 27]. All the three possible configurations, the dipole (see Ref. [20, 49, 21, 50]), the Saturn ring (see Ref [51]), and the surface ring (see Ref. [52]) have been seen in experiments.

2.2.2. *The Twisted Dipole Configuration*

A careful numerical study of the dipole configuration as a function of the reduced splay (K_1/K_2) and twist (K_2/K_3) constants reveals the following picture illustrated in Fig. 4. For large twist constants, the dipole configuration occurs as drawn in Fig. 3. The distance r_d of the defect from the center of the sphere does hardly depend on the elastic constants. Its value $r_d = 1.26 \pm 0.02$ agrees very well with analytic calculations based on a generalized electric-field ansatz [26]. As the twist constant is lowered or the splay constant is increased, a twisted dipole configuration evolves. Figure 5 shows the new structure where the directors close to the hyperbolic hedgehog are tilted relative to the drawing plane. Furthermore, it is found that the sphere-defect distance r_d starts to grow beyond the twist transition line. The twisted dipole should appear in typical calamatic liquid crystals like MBBA, 5CB, and PAA (see Fig. 4), and it should be visible under a polarizing microscope when viewed along its symmetry axis.

The twist transition breaks the mirror symmetry of the dipole, which

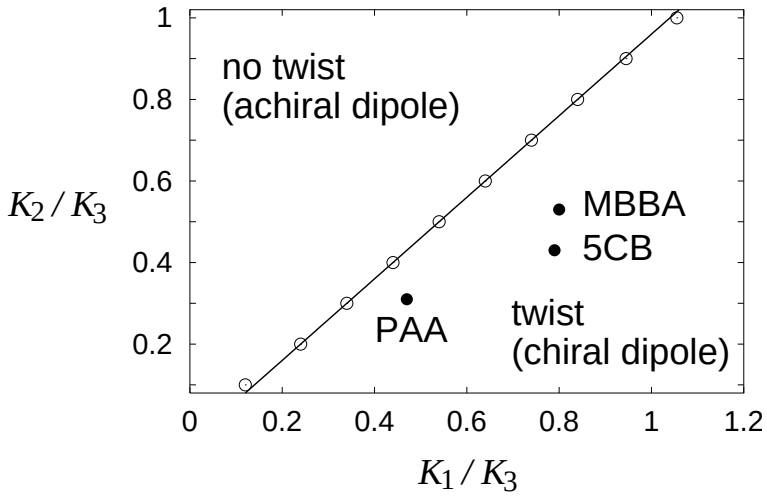

Figure 4. Phase diagram of the twist transition as a function of the reduced splay (K_1/K_3) and twist (K_2/K_3) constants.

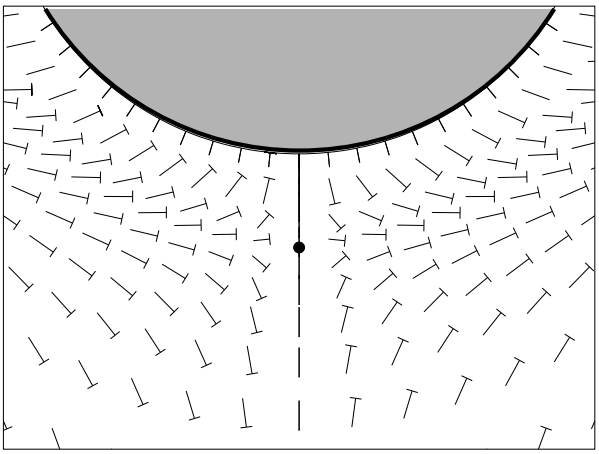

Figure 5. Nail picture of a close-up of the twisted dipole configuration. Around the hyperbolic hedgehog the directors are tilted relative to the drawing plane.

then becomes a chiral object. This is an interesting example of a symmetry breaking phase transition. Since left and right-handed dipole have the same energy, the transition should be of second order as predicted by a conventional Landau expansion of the free energy in an appropriate twist order parameter [27].

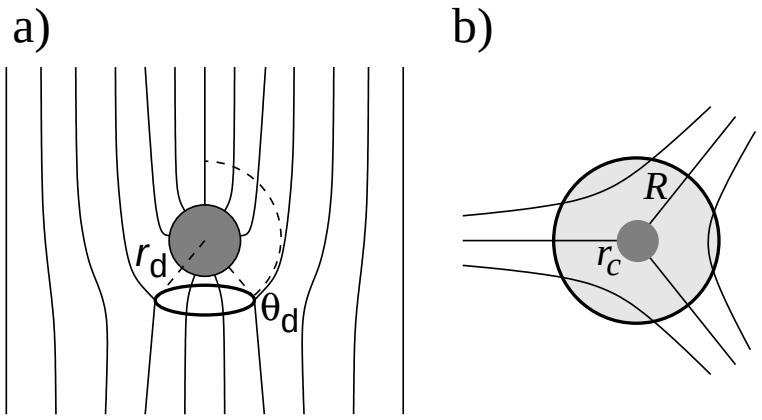

Figure 6. a) Coordinates (r_d, θ_d) for a $-1/2$ disclination ring with a general position around the spherical particle; b) Circular cross section of the $-1/2$ disclination ring with radius R and core radius r_c.

2.2.3. *Dipole versus Saturn ring*

Ring disclinations:
The energy of the hyperbolic point defect is not correctly calculated in the numerical treatment since the Frank free energy does not apply in its core. However, a good approximation for the core energy is $K_3 \times r_c$ where $r_c = 10\,\text{nm}$ denotes the radial extension of the core [53]. Since the free energy of the dipole amounts to around $10\pi K_3 a$, where a is the particle radius, we can consider particle sizes down to 100 nm still keeping the energy contribution of the point defect smaller than 1 %. This is beyond the numerical accuracy, and therefore no energetical correction for the point defect is included.

The situation for ring defects is different since the line energy of the core is of the order of K_i. As starting configuration in the numerical minimization, an analytical form of the director configuration of a $-\frac{1}{2}$ disclination ring around a spherical particle is taken (see Ref. [26]). The general position of this ring is determined by the radial (r_d) and the angular (θ_d) coordinates as illustrated by Fig. 6a). During the relaxation the disclination ring $(\theta_d \neq 0, \pi)$ basically stays at the position where it is placed. There seems to be a "numerical" barrier for the defect to cross a grid line. This phenomenon is used to investigate the free energy as a function of r_d and θ_d which gives an instructive insight into potential barriers for a transition between dipole and Saturn-ring configuration. The results are equivalent to determining the director field for a fixed position of the disclination ring. Again, the numerical integration of the Frank free energy $F_{\mathbf{n}}$ does not give the right energy of the disclination. To correct this deficieny, we use the

formula

$$F = F_{\mathbf{n}} - F_{\mathbf{n}}|_{\text{torus}} + F_{c/d} \times 2\pi r_d \sin\theta_d \ . \tag{15}$$

The quantity $F_{\mathbf{n}}|_{\text{torus}}$ denotes the numerically calculated free energy of a toroidal region of cross section πR^2 around the disclination ring [see Fig. 6b)]. Its volume is $\pi R^2 \times 2\pi r_d \sin\theta_d$, where the coordinates (r_d, θ_d) of the ring are determined by searching for the maximum of the Frank free energy density f_{el}. The value of $F_{\mathbf{n}}|_{\text{torus}}$ is replaced by the last term on the right-hand side of Eq. (15), where

$$F_d = \frac{\pi}{4} K \left(\frac{1}{2} + \ln \frac{R}{r_c} \right) \tag{16}$$

is the line energy of a $\pm\frac{1}{2}$ disclination in the one-constant approximation ($K_i = K$) with its core and elastic contribution [22]. Note that Eq. (16) is not valid if a magnetic field $\mathbf{H}$ is applied. In the general case ($K_1 \neq K_2 \neq K_3$) an analytic expression for the elastic energy does not exist. However, one can use a rough approximation for the core line energy F_c by averaging over the Frank constants:

$$F_c = \frac{\pi}{8}(K_1 + K_2 + K_3)/3 \ . \tag{17}$$

It should also apply to $H \neq 0$. To find out how large the cross section πR^2 of the cut torus has to be, the formula (15) and the line energy of Eq. (16) are employed for constant r_c and varying R. To be consistent, the free energy F should not depend on R. Within an error of less than 1 %, this is the case if πR^2 is equal or larger than $3\Delta\rho\Delta\theta/2$ where $\Delta\rho$ and $\Delta\theta$ are the lattice constants of the grid and $\rho = 1/r^2$ is the modified radial coordinate in units of $1/a^2$ (see Subsection 2.1.2). To study the transition between the dipole and the Saturn ring as a function of particle size, $\pi R^2 = 25\Delta\rho\Delta\theta/2$ is chosen and Eq. (16) is employed for different r_c. When a magnetic field is applied, $R = r_c$ is determined from $\pi r_c^2 = 3\Delta\rho\Delta\theta/2$, and the core energy of Eq. (17) is used.

By performing the correction for the line energy of the disclination ring, a second length scale besides the particle radius a enters in our problem: the core radius $r_c = 10\,\text{nm}$. This explains the physical mechanism, why the director configuration around a particle should depend on its size. If finite surface anchoring is assumed, or if a magnetic field is applied further length scales exist. They were already introduced in Subsection 2.1.1.

Effect of particle size:
In Fig. 7 the free energy F in units of $\pi K_3 a$ is plotted as a function of

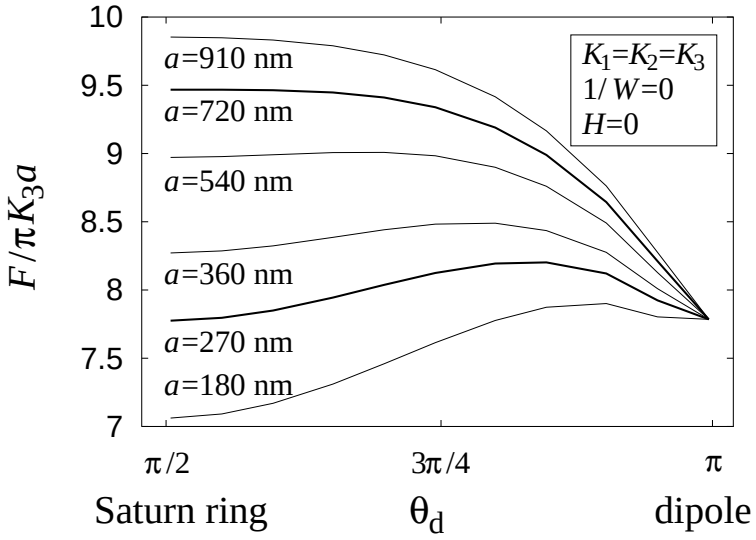

Figure 7. The free energy F in units of $\pi K_3 a$ as a function of the angular coordinate θ_d. The parameter of the curves is the particle size a. Further parameters are indicated in the inset.

the angular coordinate θ_d of the disclination ring. For constant θ_d, the free energy F was chosen as the minimum over the radial coordinate r_d. The particle radius a is the parameter of the curves, and the one-constant approximation is employed. Recall that $\theta_d = \pi/2$ and $\theta_d = \pi$ correspond, respectively, to the Saturn-ring or the dipole configuration. Clearly, for small particle sizes ($a = 180\,\mathrm{nm}$) the Saturn ring is the absolutely stable configuration, and the dipole enjoys some metastability. However, thermal fluctuations cannot induce a transition to the dipole since the potential barriers are much higher than the thermal energy $k_\mathrm{B}T$. *E.g.*, a barrier of $0.1\pi K_3 a$ corresponds to $1000\,k_\mathrm{B}T$ ($T = 300\,\mathrm{K}$, $a = 1\,\mu\mathrm{m}$). At $a \approx 270\,\mathrm{nm}$, the dipole assumes the global minimum of the free energy, and finally the Saturn ring becomes unstable at $a \approx 720\,\mathrm{nm}$. The scenario agrees with the results of Ref. [26] where an ansatz function for the director field was used.

For the reduced radial coordinate of the disclination ring, one finds $r_d/a = 1.12$ for 270 nm particles and $r_d/a = 1.10$ for 720 nm particles, indepent of the angular coordinate. Only in the region where the ring closes to the hyperbolic hedgehog, does r_d increase sharply to the value of 1.26. Note that smaller spheres push the ring further away from the surface. The radial position $r_d/a = 1.10$ agrees very well with analytical results obtained by using an ansatz function (see Ref. [26]) and with numerical calculations based on a Monte-Carlo minimization [54].

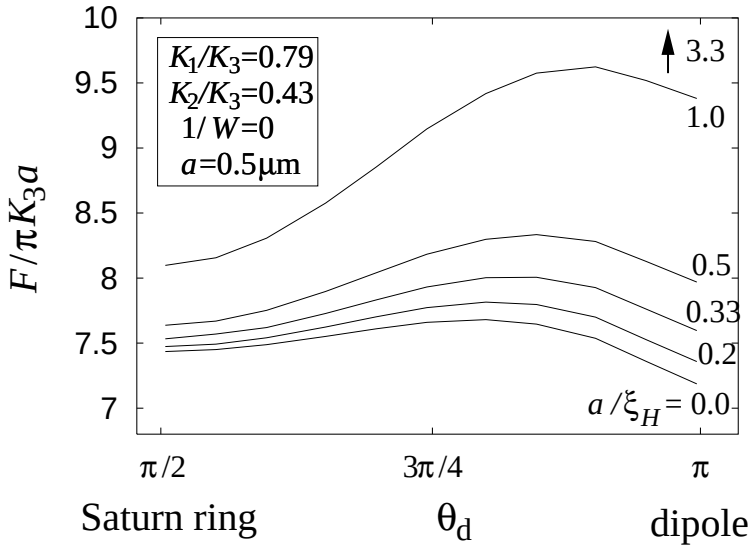

Figure 8. The free energy F in units of $\pi K_3 a$ as a function of the angular coordinate θ_d. The parameter of the curves is the reduced inverse magnetic coherence length a/ξ_H. Further parameters are indicated in the inset.

Effect of a magnetic field:
A magnetic field applied along the symmetry axis of the dipole can induce a transition to the Saturn-ring configuration. This can be understood from a simple back-of-the-envelope calculation. Let us consider high magnetic fields, *i.e.*, magnetic coherence lengths ξ_H much smaller than the particle size a. For $\xi_H \ll a$, the directors are basically aligned along the magnetic field. In the dipole configuration, the director field close to the hyperbolic hedgehog cannot change its topology. The field lines are "compressed" along the symmetry axis, and high densities of the elastic and magnetic free energies occur in a region of thickness ξ_H. Since the field lines have to bend around the sphere, the cross section of the region is of the order of a^2, and its volume is proportional to $a^2\xi_H$. The Frank free energy density is of the order of K/ξ_H^2, where K is a typical Frank constant, and therefore the elastic free energy scales with Ka^2/ξ_H. The same holds for the magnetic free energy. In the case of the Saturn-ring configuration, high free energy densities occur in a toroidal region of cross section $\propto \xi_H^2$ around the disclination ring. Hence, the volume scales with $a\xi_H^2$, and the total free energy is of the order of Ka, *i.e.*, a factor a/ξ_H smaller than for the dipole.

Figure 8 presents a calculation for a particle size of $a = 0.5\,\mu$m and the liquid crystal compound 5CB. We plot the free energy in units of $\pi K_3 a$ as a function of θ_d for different magnetic field strengths which we indicate

by the reduced inverse coherence length a/ξ_H. Without a field ($a/\xi_H = 0$), the dipole is the energetically preferred configuration. The Saturn ring shows metastability. A thermally induced transition between both states cannot happen because of the high potential barrier. At a field strength $a/\xi_H = 0.33$, the Saturn ring becomes the stable configuration. However, there will be no transition until the dipole loses its metastability at a field strength $a/\xi_H = 3.3$, which is only indicated by an arrow in Fig. 8. Once the system has changed to the Saturn ring, it will stay there even for zero magnetic field. Hence, the dipole is transformed into a Saturn ring with the help of a magnetic field. If the Saturn ring is unstable at zero field, a hysteresis occurs. Starting from high magnetic fields, the Saturn ring loses its metastability at a certain field strength, and a transition back to the dipole takes place. In Fig. 7, it was shown that the second situation is realized for particles larger than 720 nm. Calculations were also performed for a particle size of 1μm and the liquid crystal compound 5CB. It was found that the Saturn ring is still metastable at zero field in contrast to the result of the one-constant approximation.

2.2.4. *Influence of Finite Surface Anchoring*

In the last subsection we investigate the effect of finite anchoring on the director field around the spherical particle. The saddle-splay term with its elastic constant K_{24} is important now. In Fig. 9 the free energy is plotted versus the reduced surface extrapolation length ξ_S/a for different reduced saddle-splay constants K_{24}/K_3. Zero magnetic field and the one-constant approximation are chosen. The straight lines belong to the dipole. Then, for decreasing surface anchoring, there is a first-order transition to the surface-ring structure. We never find the Saturn ring to be the stable configuration although it enjoys some metastability. For $K_{24}/K_3 = 0$, the transition takes place at $\xi_S/a \approx 0.085$. This value is somewhat smaller than the result obtained by Ruhwandl and Terentjev [54]. One could wonder why the surface ring already occurs at such a strong anchoring like $\xi_S/a \approx 0.085$ where any deviation from the homeotropic anchoring costs a lot of energy. However, if $\Delta\theta$ is the angular width of the surface ring where the director deviates from the homeotropic alignment, then a simple energetical estimate allows $\Delta\theta$ to be of the order of ξ_S/a.

It is interesting to see that the transition point shifts to higher anchoring strengths, *i.e*, decreasing ξ_S/a when K_{24}/K_3 is increased. Obviously, the saddle-splay term favors the surface-ring configuration. This fact can be understood immediately since the surface ring at the equator of the sphere introduces a "saddle" in the director field. Such a structure is known to be favored by the saddle-splay term. The conclusion can be checked by the numerical calculation and an analytical modelling of the surface ring [27].

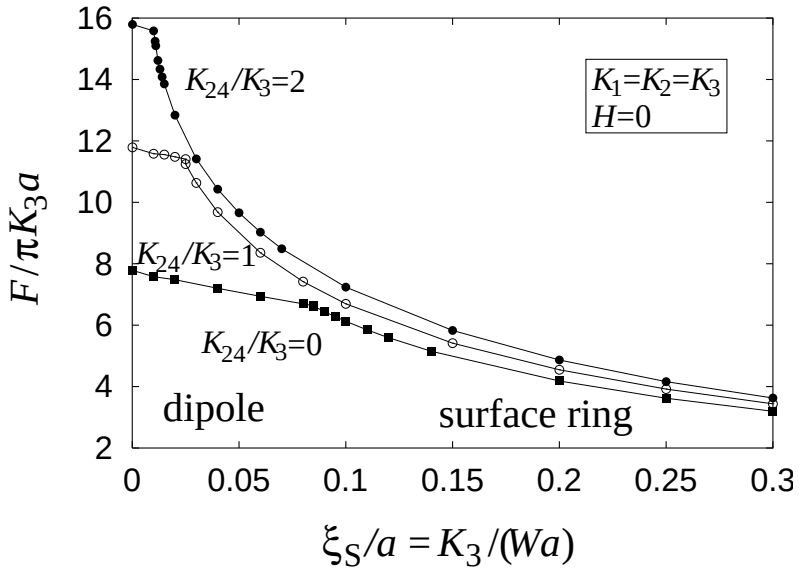

Figure 9. The minimum free energy F in units of $\pi K_3 a$ as a function of the reduced surface extrapolation length ξ_S/a for different K_{24}/K_3. A first-order phase transition from the dipole to the surface ring occurs. Further parameters are indicated in the inset.

2.3. TWO-PARTICLE INTERACTIONS IN A NEMATIC SOLVENT

Two particles in a nematic solvent interact since the director field between particles is distorted. To calculate the two-particle interaction exactly, one has to determine the director field around two spheres by minimizing the Frank free energy. An analytical approch would require appropriate ansatz functions which are not known so far. A pure numerical approach becomes difficult when the particles are far away from each other since the integration volume becomes very large. Here we are especially interested in the long-range character of the interaction, and a phenomenological approach is chosen to determine it.

It is instructive to first consider the director field far away from the particle, which crucially depends on the global symmetry of the system [55, 26]. Let the director $\mathbf{n}_0$ at infinity point along the z axis. Then, in the far field, the director is approximated by $\mathbf{n}(\mathbf{r}) \approx (n_x, n_y, 1)$ with $n_x, n_y \ll 1$. In leading order, the normalization of the director can be neglected, and the Euler-Lagrange equations for n_x and n_y arising from a minimization of the Frank free energy in the one-constant approximation are simply Laplace equations, $\nabla^2 n_\mu = 0$. The solutions are the well-known multipole expansions of electrostatics that include monopole, dipole, and quadrupole terms. They are all present if the suspended particle has a general shape or

if, *e.g.*, the dipole in Fig. 3 is tilted against $\mathbf{n}_0$. In the dipole configuration with its axial symmetry about $\mathbf{n}_0$, the monopole is forbidden, and one obtains

$$n_x = p\,\frac{x}{r_3} + 2c\,\frac{zx}{r^5} \qquad \text{and} \qquad n_y = p\,\frac{y}{r_3} + 2c\,\frac{zy}{r^5}\ , \tag{18}$$

where $r = (x^2 + y^2 + z^2)^{1/2}$. The expansion coefficients p and c are determined by minimizing the Frank free energy. They are used to assign both a dipole ($\mathbf{p}$) and quadrupole ($\mathbf{c}$) moment to the configuration:

$$\mathbf{p} = p\,\mathbf{n}_0 \qquad \text{and} \qquad \mathbf{c} = c\,(\mathbf{n}_0 \otimes \mathbf{n}_0 - \mathbf{1}/3)\ . \tag{19}$$

The symbol $\otimes$ means tensor product, and $\mathbf{1}$ is the unit tensor of second rank. We adopt the convention that the dipole moment $\mathbf{p}$ points from the companion defect to the particle. Hence, if $p > 0$, the far field of Eqs. (18) belongs to a dipole configuration with the defect sitting below the particle (see Fig. 3). Saturn-ring and surface-ring configurations possess a mirror plane perpendicular to the rotational axis. Therefore, the dipole term in Eqs. (18) is forbidden, *i.e.*, $p = 0$.

In the following we concentrate on the dipole configuration. A thorough discussion of the two-particle interactions is presented in Ref. [26]. We introduce a dipole-moment density of particle-defect dipoles situated at $\mathbf{r}^\alpha$,

$$\mathbf{P}(\mathbf{r}) = \sum_\alpha \mathbf{p}^\alpha \delta(\mathbf{r} - \mathbf{r}^\alpha) \qquad \text{with} \qquad \mathbf{p}^\alpha = p\mathbf{e}^\alpha\ . \tag{20}$$

The unit vector $\mathbf{e}^\alpha$ specifies the direction of the dipole moment associated with droplet α. It can differ from the director $\mathbf{n}_0$ far away from the particle which means that the particle-defect dipole is tilted against $\mathbf{n}_0$. In constructing $\mathbf{P}(\mathbf{r})$, the particles are regarded as point objects. Hence the theory formulated in the following is only valid at length scales large compared to the particle radius. Now, a free energy is constructed from all rotationally invariant combinations of $\mathbf{P}$, $\mathbf{n}$, and the gradient operator ∇ that are also even under $\mathbf{n} \to -\mathbf{n}$. The result is

$$\begin{aligned} F \;=\; & \frac{K}{2}\int d^3r\,(\nabla_i n_j)^2 - A\sum_\alpha [\mathbf{p}^\alpha \cdot \mathbf{n}(\mathbf{r}^\alpha)]^2 \\ & + 4\pi K \int d^3r [-\mathbf{P}\cdot\mathbf{n}(\nabla\cdot\mathbf{n}) + \gamma\mathbf{P}\cdot(\mathbf{n}\times\nabla\times\mathbf{n})]\ . \end{aligned} \tag{21}$$

The first term on the right-hand side is the conventional Frank elastic free energy in the one-constant approximation. The second term demands

that the particle-defect dipole prefers to be parallel to the local director $\mathbf{n}(\mathbf{r}^\alpha)$. According to the restriction of the theory to length scales large compared to the particle radius, this is the director $\mathbf{n}_0$ far away from the particle. The third and fourth term are identical to the treatment of the flexoelectric effect in a nematic [56, 37]. The $-\mathbf{P}\cdot\mathbf{n}(\nabla\cdot\mathbf{n})$ term in Eq. (21) shows that dipoles aligned along $\mathbf{n}$ create local splay as is evident from the dipole configuration depicted in Fig. 3. In addition, this term predicts that dipoles can lower their energy by migrating to regions of maximum splay while remaining aligned with the local director. Experiments on multiple nematic emulsions [20, 21] support this conclusion. Indeed, the coupling of the dipole moment to a strong splay distortion explains the chaining of water droplets in a large nematic drop whose observation was reported in the introduction. This subject will be addressed further in the next subsection. The dipole-bend coupling term in Eq. (21) does not contribute in the following treatment.

We now assume that the far-field director $\mathbf{n}_0$ and all the dipole moments of the particles point along the z axis, *i.e.*, $\mathbf{P}(\mathbf{r}) = P(\mathbf{r})\mathbf{n}_0$. Furthermore, we are interested in small deviations from $\mathbf{n}_0$, $\mathbf{n} = (n_x, n_y, 1)$, and formulate the effective energy of Eq. (21) up to harmonic order in n_μ:

$$F = K \int d^3r \, [\tfrac{1}{2}(\nabla n_\mu)^2 - 4\pi P \partial_\mu n_\mu] \ . \tag{22}$$

The Euler-Lagrange equations for the director components are

$$\nabla^2 n_\mu = 4\pi \partial_\mu P(\mathbf{r}) \ , \tag{23}$$

which possess the solution

$$n_\mu(\mathbf{r}) = -\int d^3r' \, \frac{1}{|\mathbf{r}-\mathbf{r}'|} \, \partial'_\mu P(\mathbf{r}') \ . \tag{24}$$

For a single droplet at the origin, $P(\mathbf{r}) = p\,\delta(\mathbf{r})$, and the equation yields exactly the dipole part of the far field in Eq. (18). This demonstrates the validity of the phenomenological approach.

Inserting the solution (24) into Eq. (22), expresses the free energy as pairwise interactions of the dipole densities,

$$\frac{F}{4\pi K} = \frac{1}{2} \int d^3r d^3r' \, P(\mathbf{r}) V_{PP}(\mathbf{r}-\mathbf{r}') P(\mathbf{r}') \ , \tag{25}$$

with

$$V_{PP}(\mathbf{r}) = \partial_\mu \partial_\mu \frac{1}{r} \ = \ \frac{1}{r^3}\,(1 - 3\cos^3\theta) \ , \tag{26}$$

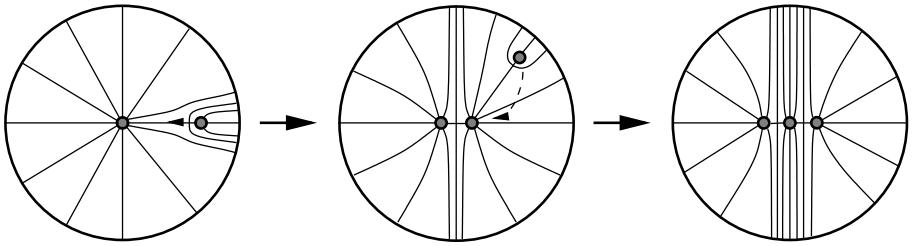

Figure 10. Scenario to explain the chaining of water droplets in a large nematic drop. The second water droplet and its companion hyperbolic hedgehog form a dipole so that the total charge of the nematic drop is not changed. The dipole is attracted by the strong splay deformation around the droplet in the center (left picture). The dipole moves towards the center until at short distances the repulsion mediated by the point defect sets in (middle picture). A third droplet moves to the region of maximum splay to form a linear chain with the two other droplets.

where θ is the angle enclosed by the separation vector $\mathbf{r}$ and $\mathbf{n}_0$. Thus, the interaction energy between particles at positions $\mathbf{r}$ and $\mathbf{r}'$ with respective dipole moments p and p' is

$$U(\mathbf{R}) = 4\pi K\, p\, p' V_{PP}(\mathbf{R}) \quad , \tag{27}$$

where $\mathbf{R} = \mathbf{r} - \mathbf{r}'$. The potential $U(\mathbf{R})$ is identical to the analogous problem in electrostatics. Minimizing it over the angle θ, one finds that the dipoles prefer to form chains along their axes, *i.e.*, $p\,p' > 0$, $\theta = 0, \pi$. The chaining was observed by Poulin *et al.* in inverted emulsions [49, 21] or in a suspension of micron-size latex particles in a lyotropic discotic nematic [50]. Poulin *et al.* also confirmed the functional form of the dipolar force (see Ref. [49]).

In the Saturn-ring and surface-ring configuration, the dipole moment is zero. A phenomenological theory including quadrupole moments predicts that they interact like electric quadrupoles [57, 26].

2.4. NEMATIC COLLOIDAL DISPERSIONS IN COMPLEX GEOMETRIES

2.4.1. *Motivation*

In Subsection 2.2 the dipole configuration was introduced under the boundary condition of a uniform director field at infinity. In Subsection 2.3 this constraint was released by demanding that the director field far away from the particle is sufficiently smooth. This enables the definition of a local director along which the dipole aligns. In the following, it is demonstrated that the particle-defect dipole also exists in more complex geomtries, e.g., nematic drops. First, we will consider the chaining of water droplets in a large nematic drop which was already introduced in the introduction and

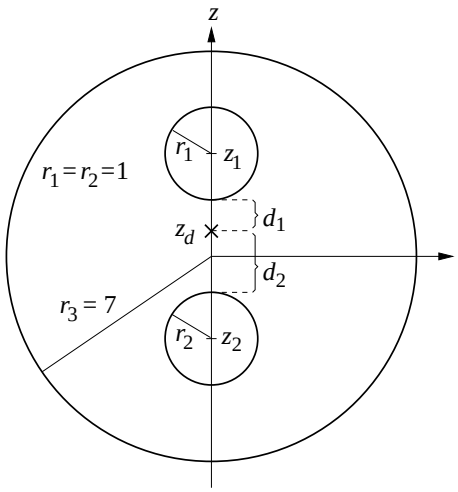

Figure 11. a) Geometry parameters for two water droplets with radii $r_1 = r_2 = 1$ in a large nematic drop with radius $r_3 = 7$. The system is axially symmetric about the z axis. The coordinates z_1, z_2, and z_d are the respective positions of the two droplets and the hyperbolic hedgehog. The two distances of the hedgehog from the surfaces of the droplets are d_1 and d_2.

Fig. 1. The existence of the dipole offers an explanation for the chaining since it is attracted by strong splay deformations, as predicted by the phenomenological theory of the last subsection. Figure 10 illustrates in detail why the chaining occurs. Secondly, we also identify the dipole in a bipolar configuration which occurs for planar boundary conditions at the outer surface of the nematic drop. Two boojums, *i.e.*, surface defects appear [58, 59, 60], and the dipole is attracted by the strong splay deformation in the vicinity of one of them [20, 21, 26].

2.4.2. *Geometry, Parameters, and Numerical Details*

Two particular geometries of axial symmetry are investigated numerically. The first problem is defined in Fig. 11: two spherical water droplets with radii $r_1 = r_2 = 1$ are situated in a large nematic drop with radius $r_3 = 7$. The whole system possesses axial symmetry so that the water droplets and the hyperbolic hedgehog, indicated by a cross, are located always on the z axis. The coordinates z_1, z_2, and z_d denote, respectively, the positions of the centers of the droplets and of the hyperbolic hedgehog on the z axis. The distances of the hedgehog from the surfaces of the two water droplets are, respectively, d_1 and d_2. Then, the quantity $d_1 + d_2$ means the distance of the two small spheres, and the point defect is situated in the middle between them if $d_1 = d_2$. At all the boundaries, rigid homeotropic anchoring of the director is assumed. Hence, any surface terms in the free energy can be

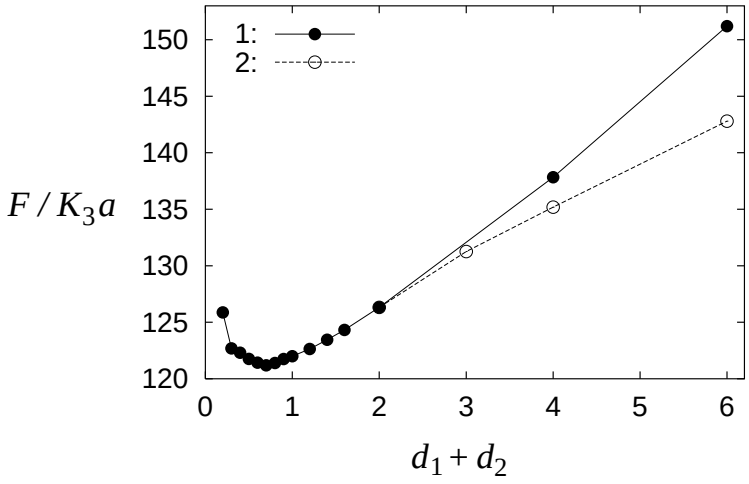

Figure 12. The free energy F as a function of the distance $d_1 + d_2$ between the small spheres which are placed symmetrically about $z = 0$. Curve 1: $z_d = 0$, curve 2: position z_d of the defect can relax along the z axis.

omitted.

In the second problem, only one water droplet inside a large nematic drop is considered. The anchoring of the director at the outer surface of the large nematic sphere is rigid planar. At the surface of the small sphere, homeotropic boundary conditions are chosen again. The same coordinates and lengths are used as described in Fig. 11 but the second droplet is omitted.

In the following, the Frank free energy is expressed in units of $K_3 a$, where a is the radius of the chaining water droplets. The starting configuration for the Newton-Gauss-Seidel method already possesses the hyperbolic point defect at a fixed position z_d. Its location does not change during the relaxation. Integrating the free energy density over one triangle of the triangulated integration area (see Fig. 2) yields a line energy. A value $F_l = (K_1 + K_3)/2$ for its upper limit is introduced. Whenever the numerically calculated local line energy is larger than F_l, it is replaced by F_l. This stabilizes the hyperbolic point defect against opening up to a disclination ring whose radius would be unphysically large. The calculations are preformed for the nematic compound 5CB with the respective bend and splay elastic constants $K_{33} = 0.53 \cdot 10^{-11}$ N and $K_{11} = 0.42 \cdot 10^{-11}$ N.

2.4.3. *Identification of the Dipole*

In Fig. 12 the free energy F is plotted as a function of the distance $d_1 + d_2$ between the surfaces of the small spheres. They are placed symmetrically

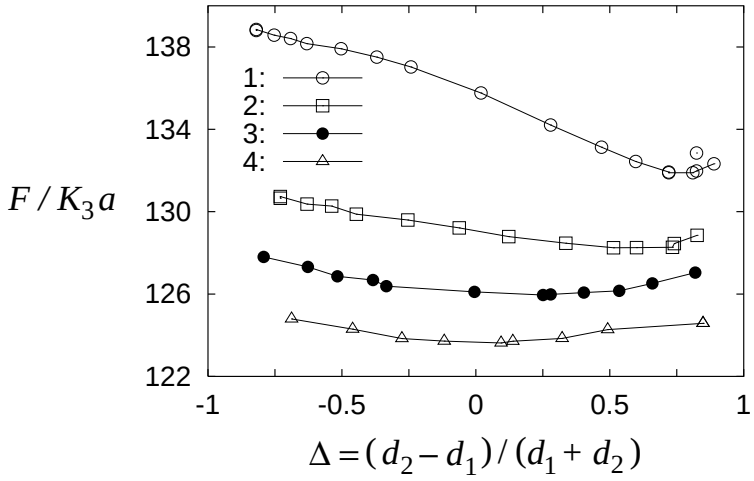

Figure 13. The free energy F as a function of $\Delta = (d_2 - d_1)/(d_1 + d_2)$. Sphere 2 is placed at $z_2 = 0$. The position z_1 of sphere 1 is the parameter. Curve 1: $z_1 = 5$, curve 2: $z_1 = 4$, curve 3: $z_1 = 3.5$, and curve 4: $z_1 = 3$.

about the center, *i.e.*, $z_2 = -z_1$. Curve 1 shows a clear minimum at $d_1 + d_2 \approx 0.7$, the defect stays in the middle between the two spheres at $z_d = 0$. In curve 2 the defect is moved along the z axis, and the minimum of the free energy is plotted for each fixed distance $d_1 + d_2$. It is obvious that beyond $d_1 + d_2 = 2$ the defect moves to one of the small spheres so that the dipole forms.

To investigate this phenomenon further, sphere 2 is placed in the center of the nematic drop at $z_2 = 0$. Then, the energetically preferred position of the point defect is determined for different locations z_1 of sphere 1. The position of the hedgehog is indicated by the order parameter $\Delta = (d_2 - d_1)/(d_1 + d_2)$. If the defect is located in the middle between the two spheres, Δ is zero since $d_1 = d_2$. On the other hand, if the defect sits at the surface of sphere 1, $d_1 = 0$, and Δ becomes one. In Fig. 13 the free energy F versus Δ is plotted. In curve 1, where the small spheres are farthest apart from each other ($z_1 = 5$), the defect is clearly close to sphere 1. This verifies that the dipole is existing. It is stable against fluctuations since a rough estimate of the thermally induced mean displacement of the defect yields 0.01. When sphere 1 is approaching the center (curve 2: $z_1 = 4$ and curve 3: $z_1 = 3.5$), the defect moves away from the droplet until it nearly reaches the middle between both spheres (curve 4: $z_1 = 3$). This means that the dipole vanishes gradually until the hyperbolic hedgehog is shared by both water droplets.

An interesting situation occurs when sphere 1 and 2 are placed sym-

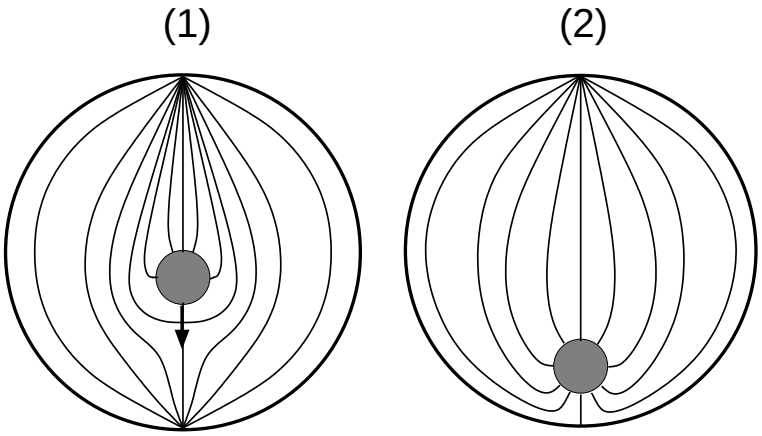

Figure 14. Planar boundary conditions at the outer surface of the large sphere create boojums, *i.e.*, surface defects at the north and the south pole. A water droplet with homeotropic boundary conditions nucleates a hyperbolic hedgehog. Two configurations exist that are either stable or metastable depending on the position of the water droplet; (1) the dipole, (2) the hyperbolic hedgehog sitting at the surface.

metrically about $z = 0$ as it was already studied in Fig. 12. Then, the defect has two equivalent positions on the positive and negative part of the z axis. Now, the situation is reminiscent to a symmetry-breaking second-order phase transition [25, 61]. It occurs when, in the course of moving the water droplets apart, the defect starts to approach one of the droplets, and the dipole forms. Take the order parameter Δ, where $\Delta = 0$ and $\Delta \neq 0$ describe, respectively, the high- and the low-symmetry phase. A Landau expansion of the free energy yields

$$F(\Delta) = F_0(z_1) + a_0[2.3 - z_1]\Delta^2 + c(z_1)\Delta^4 \ , \tag{28}$$

where $z_1 = -z_2$ plays the role of temperature, and the transition point $z_1 = 2.3$ was determined by a numerical treatment [28]. Odd powers in Δ are not allowed because of the required symmetry, $F(\Delta) = F(-\Delta)$. This free energy qualitatively describes the situation which should be observable in an experiment.

2.4.4. *The Dipole in a Bipolar Configuration*

In multiple nematic emulsions it is possible to change the anchoring of the director at the outer surface of the large nematic drop from homeotropic to planar [20]. Then the bipolar configuration for the director field appears [59, 60], where two boojums [58], *i.e.*, surface defects of charge 1 are situated at the north and south pole of the large nematic drop (see configuration (1) in Fig. 14). The topological point charge of the interior of the nematic drop

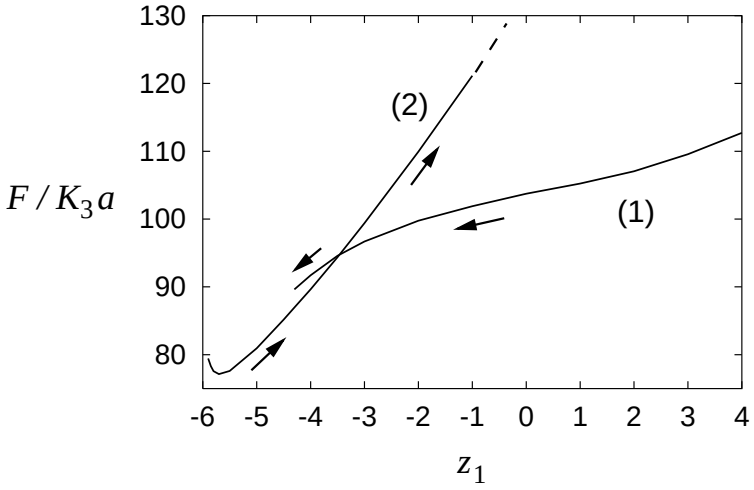

Figure 15. The free energy $\overline{F}$ as a function of the position z_1 of the water droplet for the configurations (1) and (2). For $z_1 > -3.5$, (1) is stable, and (2) is metastable. The situation is reversed for $-4.3 < z_1 < -3.5$. Configuration (1) looses its metastability at $z_1 = -4.3$.

is zero, and every small water droplet with homeotropic boundary condition has to be accompanied by a hyperbolic hedgehog. In the experiment the hedgehog sits close to the water droplet, *i.e.*, the dipole exists and it is attracted by the strong splay deformation close to the south pole [20], as predicted by the phenomenological theory of Subsection 2.3 (see also Refs. [20, 26]).

A numerical analysis of the free energy F is in agreement with experimental observations but also reveals some interesting details which have to be confirmed. In Fig. 15 the free energy F is plotted as a function of the position z_1 of the small water droplet. The diagram consists of curves (1) and (2), which correspond, respectively, to configurations (1) and (2) in Fig. 14. The free energy possesses a minimum at around $z_1 = -5.7$. The director field assumes configuration (2), where the hyperbolic hedgehog is situated at the surface of the nematic drop. Moving the water droplet closer to the surface, induces a repulsion due to the strong director deformations around the point defect. When the water droplet is placed far away from the south pole, *i.e.*, at large z_1, the dipole of configuration (1) forms and represents the absolute stable director field. At $z_1 = -3.5$ the dipole becomes metastable but the system does not assume configuration (2) since the energy barrier the system has to overcome by thermal activation is much too high. By numerically calculating the free energy for different positions of the hedgehog, we have, *e.g.*, at $z_1 = -4.0$, determined an energy barrier of

$K_3 a \approx 1000\, k_B T$, where k_B is the Boltzmann constant, T the room temperature, and $a \approx 1\,\mu$m. At $z_1 = -4.3$, the dipole even loses its metastability, the hyperbolic defect jumps to the surface at the south pole, and the water droplet follows until it reaches its energetically preferred position. On the other hand, if it were possible to move the water droplet away from the south pole, the hyperbolic hedgehog would stay at the surface since configuration (2) is always metastable for $z_1 \geq -3.5$. The energy barrier for a transition to the dipole is again at least 1000 $k_B T$ and cannot be overcome.

3. Colloidal Dispersions above the Nematic-Isotropic Phase Transition

Above T_{NI} the liquid crystal mediated interaction is short range and has a completely different spatial and temperature dependence as the one in the nematic phase. The difference between the two interactions was nicely demonstrated in an experiment performed by Poulin *et al.*[20] where it was shown that spherical water droplets immersed in a nematic liquid crystal form a long living chain of droplets. However, as the temperature was raised above T_{NI} the structure became unstable, water droplets have collapsed and formed one large droplet. The aim of this section is to explain this experiment and to predict the behavior of liquid crystal colloidal dispersions for $T > T_{NI}$.

In the isotropic phase there is no dominating long range liquid crystal mediated interaction. Therefore one has to know the details of all the relevant interactions in the system in order to determine the conditions required for the stability of isotropic liquid crystal colloidal dispersions. Besides the conventional van der Waals, screened Coulomb, and steric interactions [1], liquid crystal mediated mean-field and fluctuation-induced Casimir forces [3, 2] as well as depletion forces in case of mixtures of small and large particles [1, 10] may play an important role. In this study in addition to "conventional" liquid interactions only the mean-field part of liquid crystal interactions will be treated. Since only very dilute systems are being examined, the description will be limited to pair interactions.

3.1. STABILITY CRITERIA FOR COLLOIDAL DISPERSIONS

Colloidal dispersions of particles interacting with short range potential can undergo a transition from a dispersed to an aggregated state. Therefore answering the question about the stability of colloidal dispersions is the most important task of colloidal physics [1]. The aggregation of particles is initiated by an attractive two-particle potential. If the attraction is large compared with the thermal energy $k_B T$, a relatively *long-living non-equilibrium*

phase[1] occurs. On the other hand, attractions that are small compared with $k_{\mathrm{B}}T$ lead to an *equilibrium phase* separation in which the particles coexist in two different phases, in a dispersed and in an aggregated state. This process of aggregation, in either limit of the interaction strength, is referred to as *flocculation* [1].

Single particles in a colloidal dispersion perform Brownian motion. Due to their attractive potential once they approach each other they form aggregates. In a non-equilibrium phase, they cannot leave the state of aggregation in the period examined while in the case of phase equilibrium, the particles coexist with equal chemical potential in the dispersed as well as in the aggregated state. The higher interaction energy of the dispersed particles is compensated by their larger contribution to entropy.

In the stability study, the term "*flocculation transition temperature*" T_{FD} defines the temperature at which the system switches from a flocculated (below T_{FD}) to a dispersed state (above T_{FD})[2]. In order to be more precise, T_{FD} is chosen as the temperature below which aggregates of particles are stable. Above T_{FD} aggregates can be, depending on the presence of a repulsive barrier, metastable or unstable. It must be stressed that the "flocculation transition" is not an ordinary phase transition.

In what follows, stability study of liquid crystal suspensions, *i.e.* dispersions of noncharged and charged spherical particles in isotropic liquid crystals, will be discussed. The density of surface charges although they are screened by the dissolved counter ions, is in addition to temperature an important control parameter of the system. Therefore, the "*flocculation phase diagram*" can be predicted. It should be stressed that this is also not an ordinary phase diagram.

In a phase diagram, where also charge density in the dispersion is included as a control parameter, the term "*flocculation end line*" can be introduced. Beyond this line, the dispersed states are absolutely stable for all temperatures above the nematic-isotropic phase transition, T_{NI}. The line will be determined by the two relevant parameters of the electrostatic repulsion, *i.e.* the surface charge density of particles and the concentration of ions in the solvent.

The next section is dedicated to noncharged liquid crystal colloidal dispersions while in the rest of the chapter spherical particles carry non zero

[1]Here, long-living means long compared with the observation time, *i.e.* hours or days. Non-equilibrium, on the other hand, refers to a phase in which the particles are aggregated.

[2]The rate of flocculation and herewith a transition from the long-living equilibrium to the non-equilibrium phase is usually controlled by the concentration of ions in the solution.

but equal surface charge.

3.2. NONCHARGED LIQUID CRYSTAL COLLOIDAL DISPERSIONS AT TEMPERATURES ABOVE T_{NI}

In noncharged dispersions of classical liquids the van der Waals interaction represents the most important contribution to the interaction. However, if the classical liquid is replaced by a liquid crystal, one has to consider the liquid crystal mediated interaction as well. As shown below, close to T_{NI} the liquid crystal mediated interaction even dominates the van der Waals interaction.

3.2.1. *Van der Waals interaction*

The expression for the effective van der Waals interaction is based on the Hamaker approach, adapted to include the retardation effects [3]. For two macroscopic spherical particles of equal radii R this interaction yields [1]:

$$Int_{VW} = -\frac{A(d)}{6}\left[\frac{2R^2}{d(d+4R)} + \frac{2R^2}{(d+2R)^2} + \ln\frac{d(d+4R)}{(d+2R)^2}\right] . \qquad (29)$$

Here d is the closest distance between the surfaces of the two particles, and $A(d)$ is a generalization of the Hamaker constant which, due to retardation effects, depends on particle separation. For equal particles made of material 1 embedded in a medium 2, $A(d)$ is given by

$$\begin{aligned} A(d) &= \frac{3}{4}k_{\mathrm{B}}T\left(\frac{\epsilon_1-\epsilon_2}{\epsilon_1+\epsilon_2}\right)^2 \qquad (30)\\ &+ \frac{3h\nu_e}{16\sqrt{2}}\frac{(n_1^2-n_2^2)^2}{(n_1^2+n_2^2)^{3/2}}\left[1+\left(d\frac{\pi^2\nu_e n_2}{2\sqrt{2}c}(n_1^2+n_2^2)^{1/2}\right)^{3/2}\right]^{-2/3}, \end{aligned}$$

[1, 81], where ϵ_1 and ϵ_2 are the zero-frequency dielectric constants of the two materials, and n_1 and n_2 are the corresponding refractive indices at ν_e. The frequency ν_e refers to the dominant ultraviolet absorption in the dielectric spectrum of the embedding medium 2. It depends on the electronic transitions in the atoms and is typically around 3×10^{15} s^{-1}.

Expression (29) can be used to describe the van der Waals interaction of rigid spherical particles composed of different types of materials like polystyrene, metal, saphire and silica, that are immersed in a liquid material. It can also be used to describe the van der Waals interaction of liquid droplets that are dispersed in a liquid solvent.

[3] A detailed explanation of this approach can be found in [79, 81]

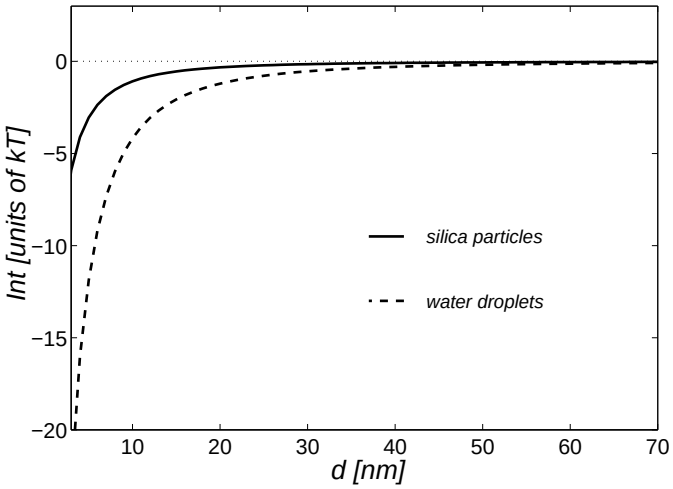

Figure 16. Van der Waals pair interaction as a function of distance between particles for silica particles and water droplets immersed into a liquid crystal. The diameter of particles is 500 nm. In the case of silica particles $\epsilon_1 = 3.8$ and $n_1 = 1.45$, while for water droplets $\epsilon_1 = 81$ and $n_1 = 1.33$. In both cases $\epsilon_2 = 11$, $n_2 = 1.57$, and $\nu_e = 3 \times 10^{15} s^{-1}$.

To specify the Hamaker constant, which determines the strength of the van der Waals interaction, the following dielectric constants and refractive indices corresponding to silica particles immersed in a typical nematic liquid crystal will be taken into account [43, 81, 85]: $\epsilon_1 = 3.8$, $n_1 = 1.45$, $\epsilon_2 = 11$, $n_2 = 1.57$, and $\nu_e = 3 \times 10^{15} s^{-1}$. As a result, the Hamaker "constant" equals $A(d) = \left(0.18 + 0.87 \left[1 + (\frac{0.12d}{\mathrm{nm}})^{3/2} \right]^{-2/3} \right) \; k_{\mathrm{B}}T$.

If instead of silica particles water droplets were dispersed in the liquid crystal, ϵ_1 and n_1 would be replaced by 81 and 1.33 respectively, and accordingly the Hamaker "constant" would be larger
$A(d) = \left(0.43 + 3.64 \left[1 + (\frac{0.11d}{\mathrm{nm}})^{3/2} \right]^{-2/3} \right) \; k_{\mathrm{B}}T$.

In figure 16 we show the spatial dependence of the van der Waals pair interaction of silica particles as well as water droplets immersed into a liquid crystal. As one can see, the van der Waals interaction exhibits an attraction which is the largest for small d and decreases to zero as the distance is increased. Note, that in the case of silica particles the van der Waals interaction is of the order of 1 $k_{\mathrm{B}}T$ or less if the distance between the particles is larger than the nematic correlation length (≈ 10 nm). The van der Waals interaction of water droplets, on the other hand, becomes smaller than 1 $k_{\mathrm{B}}T$ if the distance between the particles is increased to 2-3 correlation lengths.

3.2.2. *Calculation of free energy in partially ordered nematic liquid*

crystals

The ordering of a confined liquid crystal can be strongly influenced by the liquid crystal-solid or liquid crystal-liquid interfaces. A properly treated surface can induce a localized nematic order in the surface layer even at temperatures that are a few Kelvin above the *nematic-isotropic phase transition temperature T_{NI} of a bulk liquid crystal.* The type of surface treatment also controls the preferred direction of the molecules in the surface layer. If this direction is perpendicular to the surface then we are dealing with *homeotropic anchoring.* This will be the type of anchoring discussed in this chapter.

In contrast to the nematic phase where the Oseen-Zöcher-Frank free energy (see Eqs. (2) and (3)) is sufficient to describe most of the situations below T_{NI}, the phenomenological Landau-de Gennes theory is needed to determine the liquid crystal mediated interaction above T_{NI}. Following this theory the bulk free energy density is expressed as a power expansion in the order parameter [62]

$$f_{bulk} = \frac{1}{2}a(T - T^*)\,\mathrm{tr}\mathbf{Q}^2 \;+\; \frac{1}{3}b\,\mathrm{tr}\mathbf{Q}^3 \;+\; \frac{1}{4}c\,(\mathrm{tr}\mathbf{Q}^2)^2 \;+\; \frac{1}{2}L_1\nabla\mathbf{Q} : \nabla\mathbf{Q}\,, \tag{31}$$

where a, b, c and T^* are temperature independent constants and T is the temperature. For a typical liquid crystal they can be taken as: $a = 0.18 \times 10^6$ J/m^3 K, b = -2.3 $\times$ 10^6 J/m^3, $c = 5.02 \times 10^6$ J/m^3, $T^* = 313.5$ K. Expression (31) is called *the one constant approximation* [62, 63] corresponding to $L_2 = L_3 = L_4 = L_5 = L_6 = 0$ [64].[4]

In expression (31), only the free energy density which is not related to the properties of the surface has been discussed. To describe the influence of the surface an additional surface coupling term

$$f_s \;=\; G\,\mathrm{tr}\,(\mathbf{Q} - \mathbf{Q}_s)^2\,. \tag{32}$$

has to be added to expression (31). This generalization of the Rapini-Papoular surface free energy (8), which was first proposed by Nobili *et al.* [65] tends to equalize the surface value of the order parameter $\mathbf{Q}$ with the preferred value given by $\mathbf{Q}_s$. The constant G determines the strength of the surface coupling.

[4]To be certain that setting $L_2 = 0$ definitely does not affect the qualitative behavior of the system, the influence of the L_2 term using the ansatz function of this section was checked (see Eq. (35)). Is was found that the curves of the interaction energy versus particle separation, presented below, were shifted to larger distances in accordance with the changing correlation length. However, the main features of the interaction were not affected.

3.2.3. *Order parameter* **Q** *profile*

When determining the spatial dependence of the order parameter **Q** our discussion is limited to colloidal particles with surfaces which induce homeotropic anchoring of molecules. Homeotropic anchoring is often achieved by attaching surfactant molecules to the surface. In the vicinity of the surface, the orientational freedom and mobility of liquid crystal molecules is reduced [66, 67, 68]. This orientational and positional anchoring of the molecules promotes a pretransitional formation of homeotropic nematic ordering in the isotropic phase of nematogenic liquid crystals. In addition smectic partial layering can be induced as well [69, 70]. This effect is strongly pronounced in liquid crystals such as 8CB and 12CB. However, in 5CB-like materials smectic layers are not found in the surface induced nematic layer formed in the isotropic phase. For the sake of simplicity the layering will be neglected in this study.

Several experiments show that also in films where no smectic layers are formed at the surface, substantial surface induced nematic ordering can appear [71, 72, 73]. To qualitatively predict the behavior of molecules at the substrates, one should first in detail know the relevant molecular interactions and then perform either a molecular dynamics study, a Monte Carlo simulation or apply a density functional approach [74, 75, 76]. Usually only qualitative predictions are needed so that one is not interested in details occurring in the surface layer. Studies of the surface induced ordering in confined liquid crystals [77, 78] indicate that a combination of a phenomenological continuum Landau-de Gennes approach together with the assumption that there is an extra surface layer of molecular thickness with constant order yields a good description of observed surface induced ordering of nematogenic liquid crystals. Properties of this molecular layer are left for future discussion so that here the surface layer is simply considered as a part of the substrate.

It must be stressed that this analysis is performed within a mean-field approximation neglecting order fluctuations. An estimate of the liquid crystalline order fluctuations between two parallel plates immersed in an isotropic liquid crystal performed by Ziherl *et al.* [7] shows that the fluctuation-induced forces usually yield only a minor correction to the mean-field values and will therefore be also left for future considerations.

Since micron-size particles play an important role in the physics of liquid crystal colloidal dispersions, the attention is focused on spheres with half a micron in diameter.

For convenience, the order parameter **Q** will be expressed in terms of the scalar order parameter S and director field $\mathbf{n}$ [62]. The bulk free energy

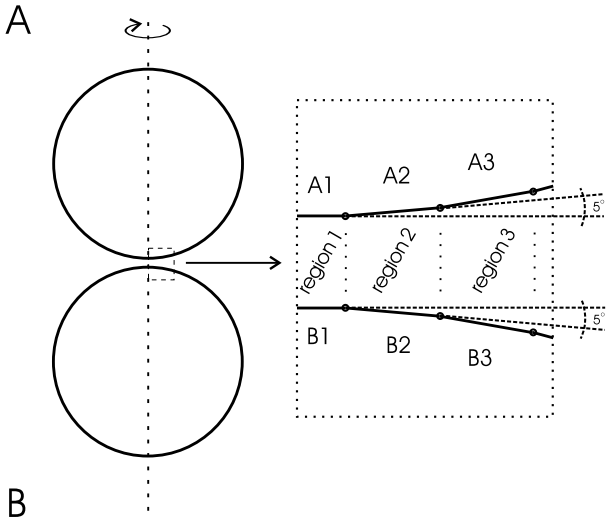

Figure 17. A model of two particles (A and B) by conical segments. As a result, the space between the particles is divided into several regions: 1,2,....

density (31) then reduces to

$$f_{bulk} = \frac{1}{2}a(T - T^*)S^2 + \frac{1}{3}bS^3 + \frac{1}{4}cS^4 + \frac{3}{2}L_1(\nabla S)^2 + \frac{9}{2}L_1 S^2 \, |\text{grad } \mathbf{n}|^2 \, . \tag{33}$$

As shown in [79] the non-harmonic terms $\frac{1}{3}bS^3$ and $\frac{1}{4}cS^4$ are unimportant in comparison to $\frac{1}{2}a(T - T^*)S^2$ if the temperature is a few K above T_{NI}. Therefore in the approximation presented here, these third and fourth-order terms will be dropped. But it will be kept in mind that at T_{NI}, the results only yield a qualitative description of the system, whereas a few K above T_{NI} also the magnitude of the results obtained will be correct.

Omitting the third and fourth-order terms in (33), and expressing the surface term (32) in terms of S and $\mathbf{n}$ the following expression for the free energy density consisting of bulk and surface terms is obtained [62]

$$\begin{aligned} f = \frac{1}{2}a\Delta T \, S^2 \quad &+ \quad \frac{3}{2}L_1(\nabla S)^2 + \frac{9}{2}L_1 S^2 \, |\text{grad } \mathbf{n}|^2 + \\ &+ \quad \left[G_S \, (\, S - S_s \,)^2 + 3G_n S S_s \, \left(1 - (\mathbf{n} \cdot \mathbf{n}_s)^2\right)\right] \delta(\left|\mathbf{r} - \vec{R}_s\right|) \, , \end{aligned} \tag{34}$$

where the surface term tends to equalize the scalar order parameter S and director $\mathbf{n}$ at the surface with their preferred values S_s and $\mathbf{n}_s$. Constants G_S and G_n determine the strength of the surface coupling.

A minimization of the free energy of the system, which is obtained by an integration of (34) over the volume occupied by the liquid crystal, yields

a system of partial differential equations. They can be solved nummericaly to obtain $S(\mathbf{r})$ and $\mathbf{n}(\mathbf{r})$ and to determine the interaction mediated by the liquid crystal. However, if some restrictions and simplifications are made, one can also obtain an analytical expression for the interaction. In the rest of the section we will introduce the procedure which leads to the analytical expression.

As a first simplification the curved surface of a spherical particle is approximated by several conical areas whose cross-sections in any plane containing the axis of symmetry are polygons of n equally long line segments as shown in Fig. 17. The region between the surfaces of the particles is devided into regions. For each region an ansatz function for the scalar order parameter as well as for the director field are constructed.

The ansatz funcion for S is just an order parameter profile between two large parallel plates which induce homeotropic anchoring

$$S = S_s \frac{\cosh z/\xi}{\cosh \overline{d}_i/2\xi + \gamma_S \sinh \overline{d}_i/2\xi} , \tag{35}$$

where $\gamma_S = 3\, L_1/(2\, G_S\, \xi)$, z is the symmetry axes of the system and d_i is the distance between two surface plates in the region. Both parameters are illustrated in region 5 of Fig. 18 (a). This approximation for the scalar order parameter can be very well justified by taking into account that S increases approximatelly exponentially with increasing distance between the plates. Therefore the interaction which originates in a partially ordered liquid crystal is only noticeable if the distance between the surfaces is not larger than approximatelly 50 nm. For a sphere with a diameter in the micrometer range this condition is only fulfilled for first few regions, where the conical surfaces are almost parallel to each other.

When choosing the ansatz for the director field, it is convenient to distinguish between two limiting cases. In the limit of a small distance between the plates, *i.e.* $d \approx \xi$, S is noticeable everywhere in the region, and the director $\mathbf{n}$ is described by a tangent vector to a circle lying in the plane which contains the axis of symmetry (see Fig. 18 (a)). In the limit of a large d ($d \gg \xi$), the two spheres do not interact. S is negligible in the middle of the zone, and the director field $\mathbf{n}$ contributes least to the free energy when it points radially outward around each sphere. Close to the $z = 0$ plane, the director fields of the two spheres are matched together by choosing $\mathbf{n}$ as the tangent vector of a circle (see Fig. 18 (b)). The size of the circle is chosen to be the same as the size of the core of a defect in the nematic phase, *i.e.*, the nematic correlation length ξ. Increasing the distance d between the two particles, the director field should change continuously from the ansatz $\mathbf{n}_o$ at a small d to the field $\mathbf{n}_\infty$ at a large d. Therefore for medium values of d,

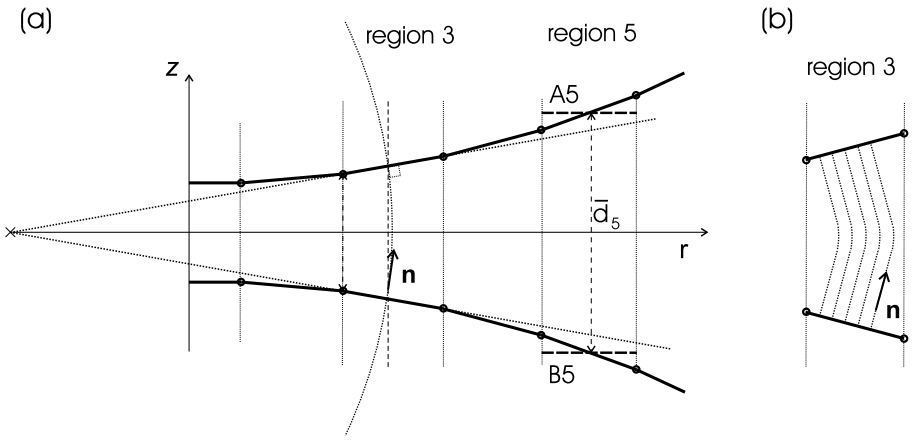

Figure 18. Illustration of the ansatz functions for S and $\mathbf{n}$. (a) In region 3 the limit of small inter-particle distances is taken into account. In this limit the director $\hat{n}$ is modelled as the tangent vector to a circle as illustrated for rigid surface anchoring. In region 5, the average distance $\overline{d}_5$ between the surface elements A_5 and B_5 is defined. (b) Illustration of the ansatz for the director field at large inter-particle distances.

the director field $\mathbf{n}$ has been chosen as a weighted superposition of $\mathbf{n}_o$ and $\mathbf{n}_\infty$.

As shown in [79] these functions represent a good approximation to the exact values of S and $\mathbf{n}$ which can be obtained by the minimization of the free energy of the system.

3.2.4. *Two particle interaction mediated by a partially ordered nematic liquid crystal*

In order to obtain an effective interaction between the two particles mediated by the surrounding liquid crystal, the free energy $F(d)$ as a function of the inter-particle distance d must be calculated. In addition, $F(d \to \infty)$ is required, where $d \to \infty$ corresponds to inter-particle separations much larger than the correlation length. The interaction can then be defined as the difference between these two quantities, $Int(d) = F(d) - F(\infty)$.

For the presentation of results, parameters corresponding to a typical nematic liquid crystal will be used, $a = 0.18 \times 10^6$ J/m^{3}K, $b = -2.3 \times 10^6$ J/m^3, $c = 5.02 \times 10^6$ J/m^3, $L_1 = 9 \times 10^{-12}$ J/m, and $T^* = 313.5$ K. The nematic-isotropic transition of a bulk liquid crystal, T_{NI} equals $T^* + 1.3$ K, while the corresponding correlation length $\xi = \sqrt{3L_1/[a(T - T^*)]}$ at T_{NI} is of the order of 10 nm. In the following, the results in terms of $T \geq T_{NI}$ will be discussed. The surface ordering parameter S_s is set at 0.3, while G_S and G_n, according to some recent data derived from experiments [77, 73], are expected to vary between 1×10^{-4} J/m^2 and 5×10^{-3} J/m^2, with the

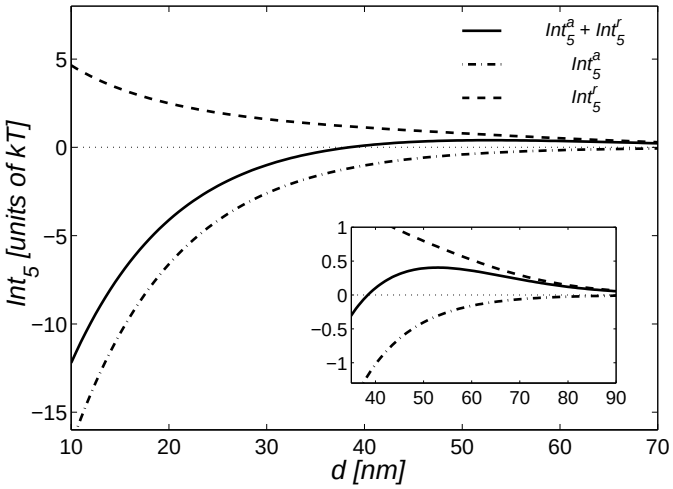

Figure 19. Attractive and repulsive contribution to the interaction in region 5 as well as their sum as a function of the inter-particle distance. The surface coupling constants G_S and G_n are 1×10^{-3}J/m^2 and 5×10^{-3} J/m^2 respectively, while $T = T_{NI}$. A magnified section of the figure is shown as inset.

ratio G_n / G_S not being larger than 5. The diameter of the particles will be set to 500 nm.

Repulsive and attractive interaction:
In the following, the interaction is divided into its attractive part resulting from the scalar order parameter S and its repulsive part originating in the elastic distortion of the director field. In Fig. 19 both contributions are illustrated for region 5 introduced in Fig. 18 (a). As parameters, $G_S = 1{\times}10^{-3}$ J/m^2, $G_n = 5{\times}10^{-3}$ J/m^2, and $T = T_{NI}$ are chosen. It is interesting to note that for a small d, the absolute value of Int_i^a is larger than Int_i^r which results in an attractive interaction. With increasing distance the attraction decreases and reaches its minimum at $d = 53$nm (see the inset of Fig. 19), beyond which the interaction becomes repulsive. In the limit of a large d, *i.e.* $d \gg \xi_{NI} \approx 10$ nm, the interaction decreases approximately exponentially.

Interaction at various temperatures:
In Figs. 20a and b, the total inter-particle interaction is shown as a function of d for various temperatures above $T^{**} = T_{NI} + 0.16$ K. The surface coupling parameters equal $G_S = 1 \times 10^{-3}$ J/m^2 and $G_n = 5 \times 10^{-3}$ J/m^2. In Fig. 20a, the range of relatively strong attraction between the parti-

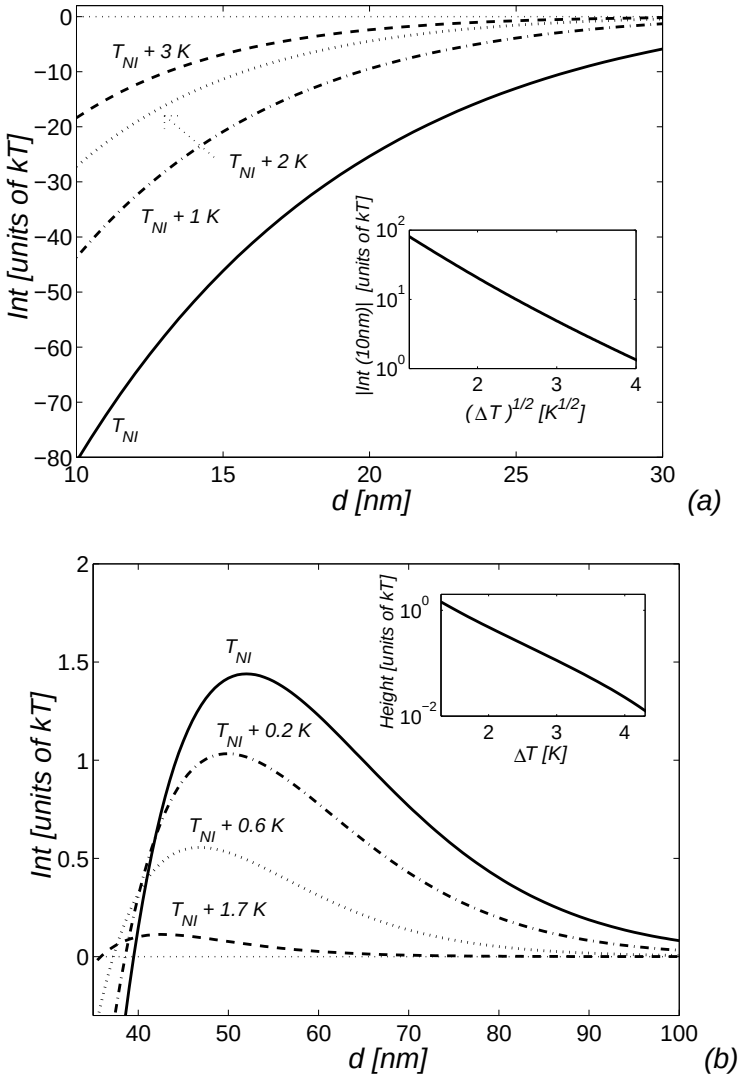

Figure 20. Two-particle interaction Int as a function of distance d between the particles at various temperatures. (a) In the range 10 nm $< d <$ 30 nm a strong attraction occurs. Inset: The absolute value of the interaction at d=10 nm is plotted in a logarithmic scale versus $\sqrt{\Delta T} = \sqrt{T - T^*}$. (b) Int($d$) in the range of the repulsion barrier, *i.e.* 35 nm $< d <$ 100 nm. Inset: The height of the repulsion barrier is plotted in a logarithmic scale versus $\Delta T = T - T^*$. Surface coupling constants G_S and G_n are 1×10^{-3} J/m^2 and 5×10^{-3} J/m^2 respectively.

cles is concentrated on, *i.e.* 10 nm $< d <$ 30 nm, while Fig. 20b presents larger distances, *i.e.* 35 nm $< d <$100 nm where the interaction exhibits a repulsion barrier.

It must be stressed that the magnitude of the interaction strongly decreases with increasing temperature for all distances d. The inset of Fig. 20a, where the absolute value of the interaction at $d = 10$ nm is plotted in a logarithmic scale versus $\sqrt{\Delta T} = \sqrt{T - T^*}$, reveals that the interaction at $d = 10$ nm is proportional to $e^{-\sqrt{\Delta T/\Delta T_\alpha}}$, where $\Delta T_\alpha = 0.4$ K is a fitting parameter. An effective distance $d_\alpha \approx 20$ nm via $\Delta T_\alpha = 3L_1/ad_\alpha^2$ is introduced, so that the exponential decrease is described by $e^{-d_\alpha/\xi(\Delta T)}$, where $\xi(\Delta T) = \sqrt{3L_1/a\Delta T}$ is the correlation length at ΔT. On the other hand, for $\Delta T < 3.5$ K the magnitude of the repulsion barrier is proportional to $e^{-\Delta T/\Delta T_\beta}$, where $\Delta T_\beta = 0.67$ K is again a fitting parameter. This can be seen in the inset of Fig. 20b, where the magnitude of the peak is plotted in a logarithmic scale versus temperature. For larger ΔT, the temperature dependence of the potential barrier height is more complicated. Because of the liquid crystal mediated interaction's relatively strong dependence on temperature, when already only a couple of K above the bulk nematic-isotropic phase transition, the attraction between the approximated particles decreases considerably, and the repulsive barrier becomes much smaller than $k_\mathrm{B}T$.

3.2.5. *Explanation of available experimental data*

The results of this interaction study can be directly applied in order to explain the experiment performed by Poulin *et al.* [20], which was briefly described at the beginning of this section. Namely, they observed that spherical liquid droplets dispersed in a nematic liquid crystal below T_{NI} form a linear chain which can persist for hours. However, when the temperature was raised above T_{NI}, the particles coagulated immediately. This phenomenon can be easily understood if one can remember that the liquid crystal mediated interaction is strongly attractive at small inter-particle distances, and exhibits a repulsive barrier that is weak in comparison with $k_\mathrm{B}T$ as the particles are moved further apart. In addition, the van der Waals interaction slightly increases the depth of the attractive part of interaction and slightly reduces the potential barrier. Since the barrier is weak, the strong attraction pulls the particles together.

In what follows it will be shown that a system of charged spherical particles immersed in an isotropic liquid crystal exhibits an additional number of interesting phenomena. In such a system, in addition to the liquid crystal mediated interaction and van der Waals attraction, electrostatic repulsion must be taken into account as well.

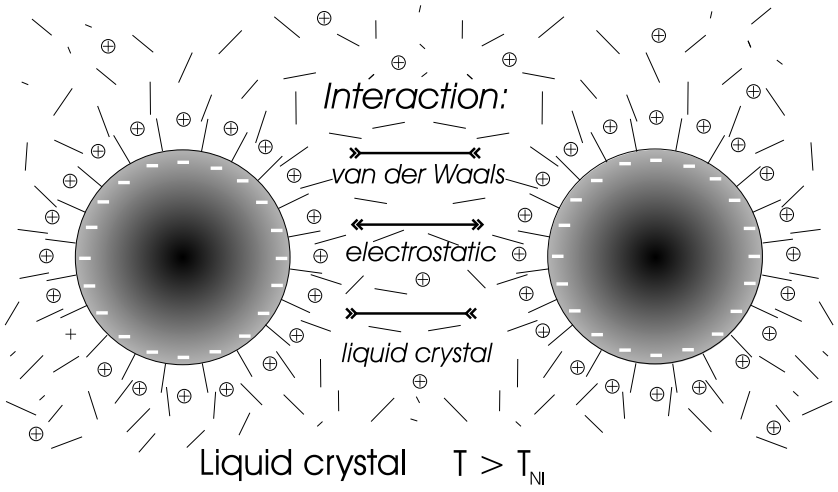

Figure 21. Charged spherical particles are immersed in a nematic liquid crystal at a temperature above the nematic-isotropic phase transition. The surface of the particles induces partial nematic ordering of the molecules, which attractively contributes to the two-particle interaction. Surface charges screened by dissolved counter ions induce a repulsive electrostatic interaction. The van der Waals interaction yields an attraction.

3.3. CHARGED SPHERICAL PARTICLES IMMERSED IN AN ISOTROPIC LIQUID CRYSTAL

As shown in section 3.2, at temperatures above T_{NI}, noncharged liquid crystals mediate a relatively strong short-range interaction which overwhelms the van der Waals attraction. In real cases colloidal dispersions include also electric charges. Therefore to describe the relevant two-particle potential in the isotropic phase, one must in addition to liquid crystal mediated and van der Walls interactions also take into account electrostatic interactions. Such a model system is schematically illustrated in Fig. 21. The most important constituents of the system are spherical particles half a micron in diameter[5], which are dispersed in the isotropic phase of a nematic liquid crystal. They carry a negative surface charge which, together with the positive free ions diluted in the solvent, gives rise to a repulsive *electrostatic interaction.* The surface of the particles is assumed to induce a perpendicular alignment of liquid crystal molecules in the surface layer. The *liquid crystal* mediates an *interaction*, which results from the distortion of the order parameter profile in the space between the two interactiong particles.

In order to find the conditions required for the stability of the liquid crystal suspension, one must be able to vary the parameters which substan-

[5]This is the typical diameter of the water droplets used in the experiment [20] which has induced this study.

tially influence the interactions: the surface charge density of particles as well as the concentration of ions in the solvent which, respectively, determine the strength and the range of the electrostatic repulsion. It is assumed that the surface charge density and the concentration of ions can be varied independently. The latter can, for example, be controlled by adding salt to the solvent.

3.3.1. *Electrostatic interaction*

According to the model presented here, all rigid spherical particles dispersed in a liquid crystal carry the same amount of surface charge. In addition, oppositely charged free ions are accumulated close to the surface. Together with the surface charge, they form an electrostatic double layer which screens the electric field produced by the surface charge. The $1/d$ dependence of the Coulomb potential, with d being the distance between the centers of two charged particles, is therefore replaced by a more complicated expression.

Following the Derjaguin approximation, the electrostatic repulsion is described by the following expression [1, 79]

$$Int_E/k_{\mathrm{B}}T = -\pi R \frac{q_s^2}{e_o^2 z^2 n_b} \ln\left(1 - e^{-\kappa d}\right) \ , \tag{36}$$

where κ is the Debye length

$$\kappa^{-1} = \sqrt{\epsilon\epsilon_o kT/2e_o^2 z^2 n_b} \tag{37}$$

d is the inter-particle distance and q_s is the surface charge density. As shown in the study of Glendinning and Russel [82], the expression (36) is valid in the limit of small inter-particle distances where $\kappa d \sim 1$, and thin double layers where $\kappa R > 30$.

To quantify the electrostatic interaction the valence, concentration of the ions dissolved in a liquid crystal, dielectric constant of the liquid crystal, and surface charge density must be specified. We assume that the ions are monovalent, *i.e.* $z = 1$ with a concentration, n_b, varying between 10^{-4} and 10^{-3} mol/l. Taking into account that the dielectric constant of the liquid crystal equals $\epsilon_2 = 11$, the corresponding Debye length at room temperature varies between 3.5 nm and 10 nm. A typical value of the surface charge density q_s is of the order of 10^4 $e_o/\mu\mathrm{m}^2$ [86]. Thus q_s will be varied between 10^3 and 10^4 $e_o/\mu\mathrm{m}^2$.

Note that the range of the surface charge densities and concentrations of ions that are taken into account in this study is small in comparison with the values that can be achieved in experiments with polar solvents. In organic solvents, however, it is generally difficult to dissolve ions. This creates

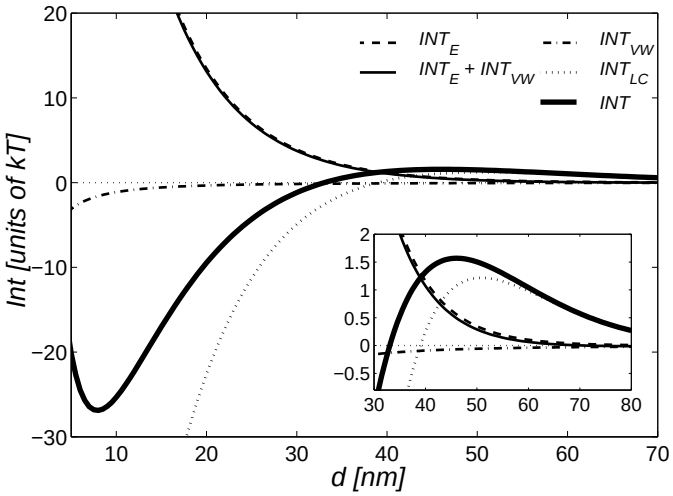

Figure 22. Electrostatic (Int_E), van der Waals (Int_{VW}), the sum $Int_E + Int_{VW}$ and liquid crystal mediated (Int_{LC}) and total ($Int = Int_{LC} + Int_{VW} + Int_E$) interactions are plotted as a function of the inter-particle distance. The surface charge density and Debye length are chosen to be $0.45 \times 10^4 e_o/\mu\text{m}^2$ and 8.3 nm respectively while $T = T_{NI} + 0.1$ K. A magnified section of the figure is shown as inset.

problems in achieving Debye lengths of the order of 10 nm. Furthermore, ionic groups attached to the surface of suspended particles do not dissociate into ions very easily, and as a result, reasonable surface charge densities cannot be obtained. Liquid crystal compounds consist of organic molecules which do, however, contain polar groups. Nevertheless, it seems that the ionic concentrations and surface charge densities employed in this study can hardly be realized. However in Ref. [87], complex salt is dissolved in nematic liquid crystals, yielding ionic concentrations of up to 10^{-4} mol/l. Furthermore, when silica spheres are coated with silan, the ionic group $NH_2^+OH^-$ occurs at the surface of the particles, with a density of 3×10^6 molecules μm^2. It also dissociates to a large amount in a liquid crystal [88]. In addition, the silan coating provides the required homeotropic boundary conditions for the liquid crystal molecules. These two examples illustrate that the parameters of the electrostatic inter-particle potential presented here should be accessible in conventional thermotropic liquid crystals.

In the following *electrostatic stabilization* will be investigated. A brief analysis will be made of the total two-particle interaction Int, which includes van der Waals (Int_{VW}), electrostatic (Int_E), and the liquid crystal mediated (Int_{LC}) interaction.

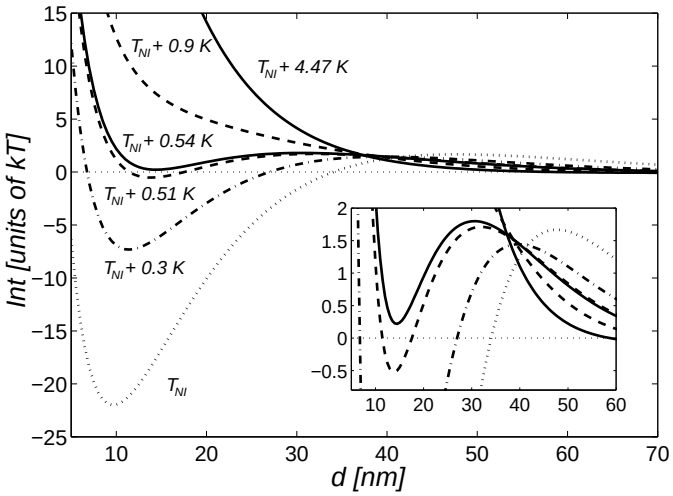

Figure 23. Interaction Int as a function of the distance between the particles for various temperatures. The surface charge density equals $0.5 \times 10^4 e_o/\mu\mathrm{m}^2$ while $\kappa^{-1} = 8.3nm$. A magnified section of the figure is shown as inset.

3.3.2. *Electrostatic stabilization of a dispersion*

Taking Int_{vdW} given by Eq.(29), Int_E described by Eq.(36) and the Int_{LC} described in Section (3.2.4) one finds the total interaction. In Fig. 22 Int_{LC}, Int_E, Int_{VW}, the sum $Int_E + Int_{VW}$, and the net interaction Int as a function of the inter-particle distance are presented. The temperature is T_{NI} + 0.1 K which is 0.06 K below T^{**}, and the surface charge density and Debye length are taken to be $0.45 \times 10^4 e_o/\mu\mathrm{m}^2$ and 8.3 nm, respectively. The electrostatic interaction exhibits a strong repulsion at small distances (d) and decreases exponentially for a large d. On the other hand, the van der Waals interaction yields an attraction of some $k_\mathrm{B}T$ at $d = 5\,\mathrm{nm}$ — much weaker than the electrostatic interaction — and decreases at $1/d^6$ for a large d. A sum of these two contributions is strongly repulsive at a small d, exhibits a shallow minimum of $1/3\ k_\mathrm{B}T$ at $d \approx 70$ nm, and approaches zero for a large d. The liquid crystal mediated interaction Int_{LC} is strongly attractive for small particle separations and weakly repulsive at $d \approx 50$ nm. It approaches zero for a large d. If this interaction is added to $Int_E + Int_{VW}$, an interaction exhibiting a deep potential minimum and a weak repulsive barrier is obtained. The minimum and the barrier appear at $d \approx 10$ nm and $d \approx 50$ nm, respectively.

Flocculation transition:

In Fig. 23, the two-particle interaction $Int = Int_{LC} + Int_{VW} + Int_E$ is

shown as a function of the particle separation for various values of temperature. The interaction curve exhibits a minimum with a depth of 10 $k_{\mathrm{B}}T$ which is followed by a low potential barrier. The potential minimum enables flocculation of particles, *i.e.*, formation of particle aggregates. Since the depth of the potential minimum as well as the height of the potential barrier are not large enough to prevent an aggregate of two particles to decay into a pair of single particles, the flocculation is a dynamical process. Particles keep forming aggregates and aggregates constantly decay back into a dispersion of single particles.

For $T = T_{NI}$, the interaction curve exhibits a minimum with a depth of the order of 20 $k_{\mathrm{B}}T$ at $d \approx 10$ nm. The minimum is followed by a small potential barrier of $\approx 1\ k_{\mathrm{B}}T$. As the temperature is raised, the depth of the minimum decreases, and already at 0.3 K, which is approximately $2(T^{**} - T_{NI})$ above T_{NI} it becomes very shallow. At $T_{NI} + 0.54\,\mathrm{K}$ the minimum still exists, but corresponds to the metastable state. The temperature at which the interaction at the minimum equals zero is called the temperature of the *"flocculation transition"*, T_{FD}. Namely, above this temperature the probability of finding two particles in an aggregated state becomes smaller than the probability that they will be dispersed. In a certain temperature interval above T_{FD}, the aggregates of particles are either unstable or metastable. When the temperature is raised even further, the interaction minimum disappears completely and the aggregates become unstable. This means that within a temperature range of a few tenth of a Kelvin, there is a sudden change from a fully aggregated to a completely dispersed state, reminiscent of the critical flocculation transition in polymer stabilized colloidal dispersions [1, 83]. We would like to stress that the flocculation of particles is a dynamical process, since the repulsive potential barrier is not high enough to prevent an aggregate of two particles to decay into two independent particles.

Since electrostatic interaction depends on the square of the surface charge density q_s, a strong electrostatic repulsion can easily be achieved. If the surface charge is large enough, the interaction at the potential minimum exceeds zero even at T_{NI}. This case is presented in Fig. 24, where a shallow minimum at T_{NI} can be observed, which disappears as the temperature is increased by 0.1 K $\approx \frac{1}{2}(T^{**} - T_{NI})$. The surface charge density and Debye length equal $q_s = 0.63 \times 10^4 e_o/\mu\mathrm{m}^2$ and κ^{-1} =8.3 nm, respectively.

"Flocculation phase diagram":
The temperature of "flocculation transition" depends strongly on the surface charge density as well as on concentration of ions in the solution. To describe this dependency, "flocculation phase diagrams" are presented in Fig. 25. Here the temperature of "flocculation transition" is plotted as a

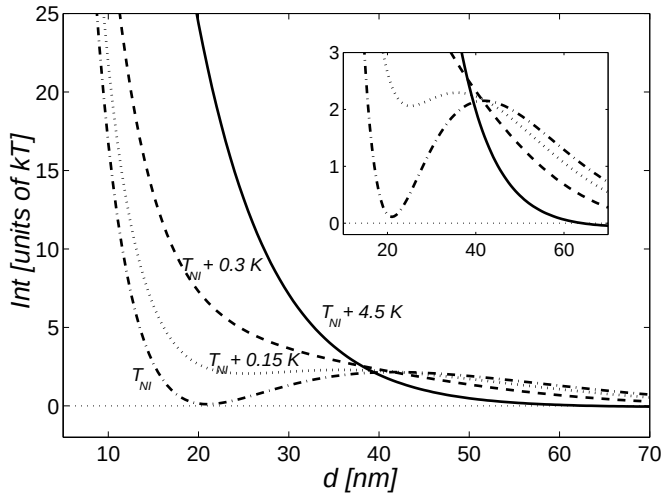

Figure 24. Interaction Int as a function of the distance between the particles for various temperatures. Surface charge density equals $0.63 \times 10^4 e_o/\mu\mathrm{m}^2$ while $\kappa^{-1} = 8.3nm$. A magnified section of the figure is shown as inset.

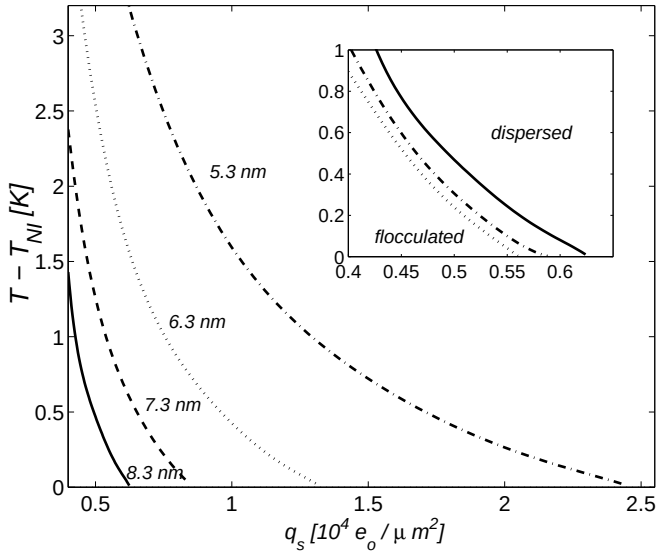

Figure 25. Temperatures of flocculation transition for various values of Debye length. A flocculation phase diagram for $\kappa^{-1} = 8.3$ nm is shown as inset. Temperatures above the temperature of flocculation transition (the solid line) correspond to the dispersed state, while for those temperatures below T_{FD}, doublets are formed. Dashed lines represent the temperatures at which the escape time is ten (dashdotted) or a hundred (dotted) times larger than in the case of zero interaction.

function of surface charge density for various values of Debye length. The regions of the dispersed or the flocculated states of particles are also indicated. The inset corresponds to the phase diagram for $\kappa^{-1} = 8.3$ nm. The solid line represents the temperatures of the "flocculation transition" T_{FD}. For temperatures above T_{FD}, the particles remain dispersed, while for temperatures below T_{FD} the system is flocculated. To obtain a feeling for the stability of the aggregated state at temperatures below T_{FD}, lines have been determined in the phase diagram, where the escape time derived from the minimum of the inter-particle potential is, respectively, ten (dash-dotted) or a hundred (dotted) times larger than in the case of zero interaction. Note that these lines are in rather close proximity to the line representing the flocculation transition. In the main plot of Fig. 25, the temperatures of the flocculation transition are shown for different values of the Debye length. A decrease of the surface charge density results in a higher transition temperature. A larger concentration of dissolved ions, *i.e.* a smaller Debye length, causes the same effect. The qualitative features of the transition lines can be easily interpreted. A smaller surface charge decreases the strength of the electrostatic repulsion, which is then compensated by a weaker attraction within the liquid crystal mediated interaction. Therefore the flocculation occurs at a higher temperature.

"Flocculation end line":
As shown in Fig. 24, large surface charge densities can even prevent the floccultion of particles at all temperatures above T_{NI}. The border line in a q_s, κ^{-1} diagram beyond which the flocculated state is never absolutely stable for all temperatures, can be defined as the "flocculation end line". It decreases very strongly with an increasing Debye length. In other words, when the the Debye length is increased as a result of a smaller ionic concentration, the screening of the surface charge q_s is reduced. Therefore, a smaller value of q_s is enough to prevent the particles from flocculating.

4. Conclusions

In this contribution we have studied liquid crystal dispersions below and above the nematic-isotropic phase transition. Below T_{NI} even one particle suspended in a nematic solvent already offers a complicated system. With the dipole, the Saturn ring and the surface ring, we have introduced the three possible configurations, and we have discussed in detail under what conditions they form. Starting from a phenomenological theory, it has been demonstrated explicitly that particles surrounded by the dipolar configuration interact like conventional dipoles. Apart from electro- or magnetorheological fluids, such a long range interaction is not present in conventional

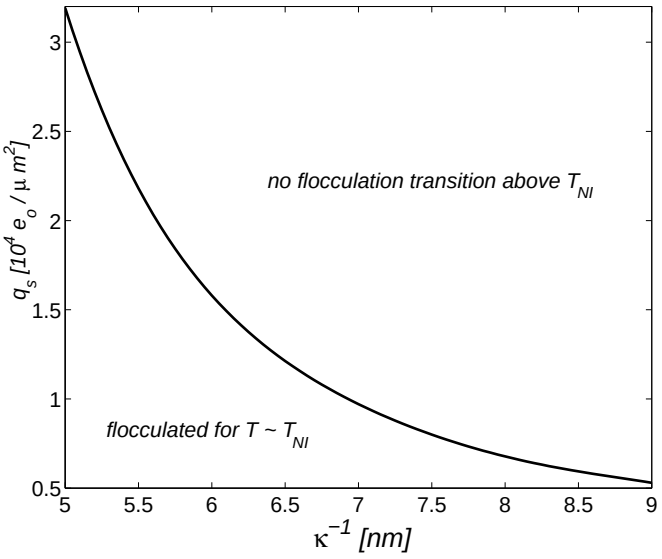

Figure 26. Flocculation end line, *i.e.* the smallest surface charge density at which particles are still dispersed at T_{NI}, as a function of the Debye length.

colloidal dispersions. It is responsible for the observed chaining of the particles. We have also addressed dispersions of particles in complex geometries, and we have studied in several situations how the dipolar configuration forms. These observations together with the finding that a magnetic or electric field can induce a transition from the dipole to the Saturn ring configuration still awaits an experimental investigation.

At temperatures above T_{NI}, the suspended particles are wetted by a surface-induced nematic film whose thickness is of the order of the nematic correlation length. The particles experience a strong liquid crystal mediated attraction when their nematic layers start to overlap since then the effective volume of liquid crystalline ordering and therefore the free energy is reduced. The attraction is short ranged and the system behaves like a conventional colloidal dispersion. Since the thickness of the nematic film increases when approaching T_{NI}, the liquid crystal mediated attraction can induce a sudden flocculation transition in an, *e.g.*, electrostatically stabilized dispersion. This phenomena is reminiscent to polymer stabilized colloids. If we use a polymer coating to stabilize the dispersion, we find that the aggregation of particles due to the liquid crystal mediated interaction sets in gradually when cooling the dispersion down towards T_c (see Ref. [30]). So far, the flocculation transition has not been studied in detail experimentally.

Liquid crystal colloidal dispersions are still a fascinating subject of ongoing research. Recent work addresses the Stokes drag of particles in a nematic solvent [89, 32, 90]. Due to the coupling of the director and the velocity field in the Ericksen-Leslie equations, the possibility of a highly non-linear Stokes drag arises [90]. Perfectly ordered chains of oil droplets in a nematic were produced from phase separation by Loudet, Barois, and Poulin [91] offering the possibility of structure formation. Meeker *et al.* reported a gel-like network in nematic colloidal dispersions with a significant shear modulus [92]. A detailed experimental and theoretical study is presented in Refs. [93, 94]. In cholesteric liquid crystals particle-stabilized defect gels were found [95], and people start to investigate dispersions of particles in a smectic phase [96, 97]. Finally, we note that the dipolar configuration also appears in two-dimensional systems including (1) free standing smectic films [98], where a circular region with an extra layer plays the role of the spherical particle, and (2) Langmuir films [99], in which a liquid-expanded inclusion in a tilted liquid-condensed region acts similarly. Theoretical studies in two dimensions were presented by Pettey, Lubensky, and Link [98].

References

1. Russel, W. B., Saville, D. A., and Schowalter, W. R. (1995) *Colloidal Dispersions*, Cambridge University Press, Cambridge.
2. Krech, M. (1994) *The Casimir Effect in Critical Systems*, World Scientific, Singapore.
3. Mostepanenko, V. M. and Trunov, N. N. (1997) *The Casimir effect and its application*, Clarendon Press, Oxford.
4. Ajdari, A., Peliti, L., and Prost, J. (March 1991) Fluctuation-Induced Long-Range Forces in Liquid Crystals, *Phys. Rev. Lett.*, **66**(11), 1481–1484.
5. Ajdari, A., Duplantier, B., Hone, D., Peliti, L., and Prost, J. (March 1992) "Pseudo-Casimir" effect in liquid crystals, *J. Phys. II France*, **2**, 487–501.
6. Swanson, B. D. and Sorenson, L. B. (October 1995) What Forces Bind Liquid Crystal, *Phys. Rev. Lett.*, **75**(18), 3293–3296.
7. Ziherl, P., Podgornik, R., and Žumer, S. (1998) Casimir force in liquid crystals close to the nematic-isotropic phase transition, *Chem. Phys. Lett.*, **295**, 99–104.
8. Dinsmore, A. D., Yodh, A. G., and Pine, D. J. (September 1996) Entropic control of particle motion using passive surface microstructures, *Nature*, **383**, 239–244.
9. Dinsmore, A. D., Wong, D. T., Nelson, P., and Yodh, A. G. (January 1998) Hard Spheres in Vesicles: Curvature-Induced Forces and Particle-Induced Curvature, *Phys. Rev. Lett.*, **80**(2), 409–412.
10. Rudhardt, D., Bechinger, C., and Leiderer, P. (August 1998) Direct Measurement of Depletion Potentials in Mixtures of Colloids and Nonionic Polymers, *Phys. Rev. Lett.*, **81**(6), 1330–1333.
11. Alder, B. J. and Wainwright, T. E. (June 1967) Velocity Autocorrelations for Hard Spheres, *Phys. Rev. Lett.*, **18**(23), 988–990.
12. Alder, B. J. and Wainwright, T. E. (1969) Enhancement of Diffusion by Vortex-Like Motion of Classical Hard Particles, *J. Phys. Soc. Jpn.*, **26**, 267–269.
13. Alder, B. J. and Wainwright, T. E. (January 1970) Decay of the Velocity Autocorrelation Function, *Phys. Rev. A*, **1**(1), 18–21.
14. Klein, R. (1997) *Interacting Brownian Particles – The Dynamics of Colloidal Sus-*

pensions, pp. 301–345, IOS Press, Amsterdam.
15. Jullien, R. and Botet, R. (1987) *Aggregation and Fractal Aggregates*, World Scientific, Singapore.
16. Meakin, P. (1988) *The Growth of Fractal Aggregates and Their Fractal Measures*, volume 12, pp. 335–489, Academic Press, New York.
17. Poon, W. C. K. and Haw, M. D. (1997) Mesoscopic structure formation in colloidal aggregation and gelation, *Adv. Colloid Interface Science*, **73**, 71–126.
18. Gast, A. P. and Zukoski, C. F. (1989) Electrorheological Fluids as Colloidal Suspensions, *Adv. Colloid Interface Science*, **30**, 153–202.
19. Liu, J., Lawrence, E. M., Wu, A., Ivey, M. L., Flores, G. A., Javier, K., Bibette, J., and Richard, J. (April 1995) Field-Induced Structures in Ferrofluid Emulsions, *Phys. Rev. Lett.*, **74**(14), 2828–2831.
20. Poulin, P., Stark, H., Lubensky, T. C., and Weitz, D. A. (March 1997) Novel Colloidal Interactions in Anisotropic Fluids, *Science*, **275**, 1770–1773.
21. Poulin, P. and Weitz, D. A. (January 1998) Inverted and multiple emulsions, *Phys. Rev. E*, **57**(1), 626–637.
22. Kléman, M. (1983) *Points, Lines and Walls: In liquid crystals, magnetic systems, and various ordered media*, John Wiley & Sons, New York.
23. Mermin, N. D. (July 1979) The topological theory of defects in ordered media, *Rev. Mod. Phys.*, **51**(3), 591–648.
24. Trebin, H.-R. (1982) The topology of non-uniform media in condensed matter physics, *Adv. Phys.*, **31**(3), 195–254.
25. Chaikin, P. and Lubensky, T. C. (1995) *Principles of Condensed Matter Physics*, Cambridge University Press, Cambridge.
26. Lubensky, T. C., Pettey, D., Currier, N., and Stark, H. (January 1998) Topological defects and interactions in nematic emulsions, *Phys. Rev. E*, **57**(1), 610–625.
27. Stark, H. (1999) Director Field Configurations around a Spherical Particle in a Nematic Liquid Crystal, *Eur. Phys. J. B*, **10**, 311–321.
28. Stark, H., Stelzer, J., and Bernhard, R. (1999) Water Droplets in a Spherically Confined Nematic Solvent: A Numerical Investigation, *Eur. Phys. J. B*, **10**, 515–523.
29. Borštnik, A., Stark, H., and Žumer, S. (1999) Interaction of spherical particles dispersed in liquid crystals above the nematic-isotropic phase transition, *Phys. Rev. E*, **60**(4), 4210–4218.
30. Borštnik, A., Stark, H., and Žumer, S. (1999) Temperature-induced flocculation of colloidal particles immersed into the isotropic phase of a nematic liquid crystal, *Phys. Rev. E*, **61**(3), 2831-2839.
31. Borštnik, A., Stark, H., and Žumer, S. (February 2000) Temperature-induced flocculation of colloidal particles immersed into the isotropic phase of a nematic liquid crystal, *Phys. Rev. E*, **61**.
32. Stark, H. (2001) Physics of Colloidal Dispersions in Nematic Liquid Crystals, *Phys. Rep.*, to be published.
33. P. Poulin, Novel phases and colloidal assemblies in liquid crystals, Current Opinion in Colloid & Interface Science **4**, 66–71 (1999).
34. Oseen, C. W. (1933) The theory of liquid crystals, *Trans. Faraday Soc.*, **29**, 883–899.
35. Zöcher, H. (1933) The Effect of a Magnetic Field on the Nematic State, *Trans. Faraday Soc.*, **29**, 945–957.
36. Frank, F. C. (1958) I. Liquid Crystals: On the Theory of Liquid Crystals, *Discuss. Faraday Soc.*, **25**, 19–28.
37. de Gennes, P. G. and Prost, J. (1993) *The Physics of Liquid Crystals*, volume 83 of *International Series of Monographs on Physics*, Oxford Science Publications, Oxford, second edition.
38. Nehring, J. and Saupe, A. (1971) On the Elastic Eheory of Uniaxial Liquid Crystals, *J. Chem. Phys.*, **54**(1), 337–343.

39. Pergamenshchik, V. M. (1998) K_{13} term and effective boundary condition for the nematic director, Phys. Rev. E, **58**(1), R16–R19.
40. Zinn-Justin, J. (1996) *Quantum Field Theory and Critical Phenomena*, volume 92 of *International Series of Monographs on Physics*, Oxford Science Publications, Oxford, third edition.
41. Morrish, A. H. (1965) *The Physical Principles of Magnetism*, Wiley Series on the Science and Technology of Materials, John Wiley & Sons, Incorporated, New York.
42. Blinov, L. M., Kabayenkov, A. Y., and Sonin, A. A. (1989) Experimental studies of the anchoring energy of nematic liquid crystals, *Liq. Cryst.*, **5**(2), 645–661.
43. Chandrasekhar, S. (1992) *Liquid Crystals*, Cambridge University Press, Cambridge, second edition.
44. Press, W. H., Teukolsky, S. A., Vetterling, W. T., and Flannery, B. P. (1992) *Numerical Recipes in Fortran: The Art of Scientific Computing*, Cambridge University Press, Cambridge.
45. Shiyanovskii, S. V. and Kuksenok, O. V. (1998) Structural transitions in nematic filled with colloid particles, *Mol. Cryst. Liq. Cryst.*, **321**, 45–56.
46. Ruhwandl, R. W. and Terentjev, E. M. (1997) Monte Carlo simulation of topological defects in the nematic liquid crystal matrix around a spherical colloid particle, *Phys. Rev. E*, **56**(5), 5561–5565.
47. Terentjev, E. M. (February 1995) Disclination loops, standing alone and around solid particles, in nematic liquid crystals, *Phys. Rev. E*, **51**(2), 1330–1337.
48. Kuksenok, O. V., Ruhwandl, R. W., Shiyanovskii, S. V., and Terentjev, E. M. (November 1996) Director structure around a colloid particle suspended in a nematic liquid crystal, *Phys. Rev. E*, **54**(5), 5198–5203.
49. Poulin, P., Cabuil, V., and Weitz, D. A. (December 1997) Direct Measurement of Colloidal Forces in an Anisotropic Solvent, *Phys. Rev. Lett.*, **79**(24), 4862–4865.
50. Poulin, P., Francès, N., and Mondain-Monval, O. (April 1999) Suspension of spherical particles in nematic solutions of disks and rods, *Phys. Rev. E*, **59**(4), 4384–4387.
51. Y. Gu and N. L. Abbott, Observation of Saturn-Ring Defects around Solid Microspheres in Nematic Liquid Crystals, Phys. Rev. Lett. **85**, 4719–4722 (2000).
52. Mondain-Monval, O., Dedieu, J. C., Gulik-Krzywicki, T., and Poulin, P. (1999) Weak Surface Energy in Nematic Dispersions: Saturn Ring Defects and Quadrupolar Interactions, *Eur. Phys. J. B*, **12**, 167–170.
53. Lavrentovich, O. and Terentév, E. (December 1986) Phase transition altering the symmetry of topological point defects (hedgehogs) in a nematic liquid crystal, *Sov. Phys. JETP*, **64**(6), 1237–1244, [Zh. Eksp. Teor. Fiz. **91**, 2084 (1986)].
54. Ruhwandl, R. W. and Terentjev, E. M. (March 1997) Long-range forces and aggregation of colloid particles in a nematic liquid crystal, *Phys. Rev. E*, **55**(3), 2958–2961.
55. Brochard, F. and de Gennes, P. G. (July 1970) Theory of Magnetic Suspensions in Liquid Crystals, *J. Phys. (Paris)*, **31**, 691–708.
56. Meyer, R. B. (May 1969) Piezoelectric Effects in Liquid Crystals, *Phys. Rev. Lett.*, **22**(18), 918–921.
57. Ramaswamy, S., Nityananda, R., Raghunathan, V. A., and Prost, J. (1996) Power-law forces between particles in a nematic, *Mol. Cryst. Liq. Cryst.*, **288**, 175–180.
58. Mermin, N. (1977) *Surface Singularities and Superflow in* ^{3}*He-A*, pp. 3–22, Plenum Press, New York.
59. Candau, S., Roy, P. L., and Debeauvais, F. (1973) Magnetic Field Effects in Nematic and Cholesteric Droplets Suspended in an Isotropic Liquid, *Mol. Cryst. Liq. Cryst.*, **23**, 283–297.
60. Kurik, M. and Lavrentovich, O. (May 1982) Negative-positive monopole transitions in cholesteric liquid crystals, *JETP Lett.*, **35**(9), 444–447, [Pis'ma Zh. Eksp. Teor. Fiz. **35**, 362 (1982)].
61. Landau, L. D. and Lifschitz, E. M. (1984) *Statistische Physik, Teil 1*, volume 5 of *Lehrbuch der Theoretischen Physik*, Akademie-Verlag, Berlin, sixth edition.
62. Priestley, E. B. Wojtowitz, P. J. and Sheng P. (1974) *Introduction to Liquid Crystals*

Plenum, New York.
63. Virga, E. G. (1994) *Variational Theories for Liquid Crystals* pp. 129, Chapman & Hall, London.
64. Kralj, S., Žumer, S. (1992) Freedericksz transitions in supra- mu m nematic droplets, *Phys. Rev. A*, **45**, 2461–2470.
65. Nobili, M. and Durand, G. (1992) Disorientation-induced disordering at a nematic-liquid-crystal-solid interface, *Phys. Rev. A*, **46**, R6174–R6177.
66. Vrbančič, N., Vilfan, M., Blinc, R., Dolinšek, J., Crawford, G. P. and Doane, J. W. (1993) Deuteron spin relaxation and molecular dynamics of a nematic liquid crystal (5CB) in cylindrical microcavities, *J. Chem. Phys.*, **98**, 3540–3557.
67. Dolinšek, J., Jarh, O., Vilfan, M., Žumer, S., Blinc, R., Doane, J. W., Crawford, G. P. (1991) Two-dimensional deuteron nuclear magnetic resonance of a polymer dispersed nematic liquid crystal, J. Chem. Phys., **95**, 2154–2161.
68. Crawford, G. P., Yang, D. K., Žumer, S., Finotello, D. and Doane, J. W. (1991) Ordering and self-diffusion in the first molecular layer at a liquid-crystal-polymer interface, *Phys. Rev. Lett.*, **66**, 723–726.
69. Ocko, B. M. (1990) Smectic-layer growth at solid interfaces, *Phys. Rev. Lett.*, **64**, 2160–2163.
70. Iannacchione, G. S., Mang, J. T., Kumar, S. and Finotello, D. (1994) Surface-induced discrete smectic order in the isotropic phase of 12CB in cylindrical pores, *Phys. Rev. Lett.*, **73**, 2708–2711.
71. Moses, T., Shen, Y. R. (1991) Pretransitional surface ordering and disordering of a liquid crystal, *Phys. Rev. Lett.*, **67**, 2033–2036.
72. Chen, W., Martinez-Miranda, L. J., Hsiung, H. and Shen, Y. R. (1989) Orientational wetting behavior of a liquid-crystal homologous series, *Phys. Rev. Lett.*, **62**, 1860–1863; (1990) Surface-induced ordering in a homologous series of liquid crystals-orientational wetting, *Mol. Cryst. Liq. Cryst.*, **179**, 419–424.
73. Crawford, G. P., Ondris-Crawford, R., Žumer, S. and Doane, J. W. (1993) Anchoring and orientational wetting transitions of confined liquid crystals, *Phys. Rev. Lett.*, **70**, 1838–1841.
74. Stelzer, J., Longa, L., Trebin, H. R. (1997) Homeotropic surface anchoring of a Gay-Berne nematic liquid crystal, *Phys. Rev. E* , **55**, 7085–7089.
75. Yoneya, M. and Iwakabe, Y. (1996) Molecular dynamics simulations of liquid crystal molecules on a polyimide monolayer, *Liq. Cryst.*, **21**, 347–359.
76. Teixeira P. I. C. (1997) Structure of a nematic liquid crystal between aligning walls, *Phys. Rev. E* , **55**, 2876–2871.
77. Crawford, G. P., Ondris-Crawford, R., Doane, J. W. and Žumer, S. (1996) Systematic study of orientational wetting and anchoring at a liquid-crystal-surfactant interface, *Phys. Rev. E* , **53**, 3647–3661.
78. Fung, Y. K., Borštnik, A. , Žumer, S., Yang, D. K. and Doane, J. W. (1997) Pretransitional nematic ordering in liquid crystals with dispersed polymer networks, *Phys. Rev. E* , **55**, 1637–1645.
79. Borštnik, A. (2000) *Interactions mediated by partially ordered nematic liquid crystals*, Ph. D. Thesis, University of Ljubljana, Ljubljana.
80. Galatola, P. and Fournier, J. B. (1999) Nematic-wetted colloids in the isotropic phase, *Mol. Cryst. Liq. Cryst.*, **330**, 1779–1783.
81. Israelachvili, J. (1992) *Intermolecular & Surface Forces*, Academic Press Limited, London.
82. Glendinning, A. B., Russel, W. B. (1983) The electrostatic repulsion between charged spheres from exact solution to the linearized Poisson-Boltzman equation, *J. Colloid Interface Sci.*, **93**, 95–104.
83. Napper, D. H. (1983) *Polymeric Stabilization of Colloidal Dispersions*, Academic Press, London.
84. Asakura, S. and Oosava, F. (1958) Interactions between particles suspended in so-

lutions of macromolecules, *J. Polym. Sci.*, **33**, 183–192.
85. Horn, R. G. (1978) Refractive indices and order parameters of two liquid crystals, *J. Physique*, **39**, 105–109.
86. Prieve, D. C. and Ruckenstein, E. (1980) Role of surface chemistry in primary and secondary coagulation and heterocoagulation, *J. Colloid Interface Sci.*, **73**, 539–555.
87. Haller, I., Young, W. R., Gladstone, G. and Teaney, D. T. (1973) Crown ether complex salts as conductive dopants for nematic liquids, *Mol. Cryst. Liq. Cryst.*, **24**, 249–258.
88. Dozov, I. private communication.
89. Ruhwandl, R. W. and Terentjev, E. M. (1996) Friction drag on a particle moving in a nematic liquid crystal, *Phys. Rev. E*, **54**, 5204–5210.
90. Stark, H. and Ventzki, D., Stokes Drag of Particles Suspended in a Nematic Liquid Crystal, in preparation.
91. Loudet, J.-C., Barois, P., and Poulin, P. (2000) Colloidal ordering from phase separation in a liquid-crystalline continuous phase, *Nature*, **407**, 611–613.
92. Meeker, S. P., Poon, W. C. K., Crain, J., and Terentjev, E. M. (2000) Colloid-liquid-crystal composites: An unusual soft solid, *Phys. Rev. E*, **61**, R6083–R6086.
93. Anderson, V. J., Terentjev, E. M., Meeker, S. P., Crain, J., and Poon, W. C. K. (2001) Cellular solid behaviour of liquid crystal colloids 1. Phase separation and morphology, *Eur. Phys. J. E*, **4**, 11-20.
94. Anderson, V. J. and Terentjev, E. M. (2001) Cellular solid behaviour of liquid crystal colloids 2. Mechanical Properties, *Eur. Phys. J. E*, **4**, 21-28.
95. Zapotocky, M., Ramos, L., Poulin, P., Lubensky, T. C., and Weitz, D. A. (1999) Particle-Stabilized Defect Gel in Cholesteric Liquid Crystals, *Science*, **283**, 209–212.
96. Jákli, A., Almásy, L., Borbély, S., and Rosta, L. (1999) Memory of silica aggregates dispersed in smectic liquid crystals: Effect of the interface properties, *Eur. Phys. J. B*, **10**, 509–513.
97. Blanc C. and Kleman M., The confinement of smectics with a strong anchoring, to be published in *Eur. Phys. J. E.*
98. Pettey, D., Lubensky, T. C., and Link, D. (1998) Topological inclusions in 2D smectic C films, *Liq. Cryst.*, **25**, 579–587.
99. Fang, J., Teer, E., Knobler, C. M., Loh, K.-K., and Rudnick, J. (1997) Boojums and the shapes of domains in monolayer films, *Phys. Rev. E*, **56**, 1859–1868.

5. Subject Index